

Feagin Rusty (Orcid ID: 0000-0002-4651-0933)  
Forbrich Inke (Orcid ID: 0000-0002-0632-7317)  
Ruiz-Plancarte Jesus (Orcid ID: 0000-0001-6736-777X)  
Fuentes Jose, D. (Orcid ID: 0000-0002-6177-6326)  
Najjar Raymond, G. (Orcid ID: 0000-0002-2960-5965)  
Vargas Rodrigo (Orcid ID: 0000-0001-6829-5333)  
Vázquez-Lule Alma (Orcid ID: 0000-0003-2919-5350)  
Windham-Myers Lisamarie (Orcid ID: 0000-0003-0281-9581)  
Kroeger Kevin, D. (Orcid ID: 0000-0002-4272-2349)  
Ward Eric, Jason (Orcid ID: 0000-0002-5047-5464)  
Leclerc Monique, Y. (Orcid ID: 0000-0002-8666-4400)  
Krauss Ken, W. (Orcid ID: 0000-0003-2195-0729)  
Stagg Camille, L (Orcid ID: 0000-0002-1125-7253)  
Alber Merryl (Orcid ID: 0000-0002-9467-4449)  
Knox Sara Helen (Orcid ID: 0000-0003-2255-5835)  
Bianchi Thomas, S. (Orcid ID: 0000-0002-3068-2933)  
Hutchings Jack, A (Orcid ID: 0000-0003-3396-6787)  
Nahrawi Hafsah (Orcid ID: 0000-0002-7400-9994)  
Noormets Askö (Orcid ID: 0000-0003-2221-2111)  
Mitra Bhaskar (Orcid ID: 0000-0002-6617-0884)  
Hinson Audra, Leigh (Orcid ID: 0000-0002-4231-4820)  
Bergamaschi Brian, A (Orcid ID: 0000-0002-9610-5581)

**Tidal wetland Gross Primary Production across the continental United States,  
2000-2019**

R.A. Feagin<sup>1</sup>, I. Forbrich<sup>2</sup>, T.P. Huff<sup>1</sup>, J.G. Barr<sup>3</sup>, J. Ruiz-Plancarte<sup>4</sup>, J.D. Fuentes<sup>4</sup>, R.G. Najjar<sup>4</sup>, R. Vargas<sup>5</sup>, A.L. Vázquez-Lule<sup>5</sup>, L. Windham-Myers<sup>6</sup>, K.D. Kroeger<sup>7</sup>, E.J. Ward<sup>8</sup>, G.W. Moore<sup>1</sup>, M. Leclerc<sup>9</sup>, K.W. Krauss<sup>8</sup>, C.L. Stagg<sup>8</sup>, M. Alber<sup>2</sup>, S.H. Knox<sup>10</sup>, K.V.R. Schäfer<sup>11</sup>, T.S. Bianchi<sup>12</sup>, J.A. Hutchings<sup>13</sup>, H. Nahrawi<sup>9,14</sup>, A. Noormets<sup>1</sup>, B. Mitra<sup>1</sup>, A. Jaimes<sup>1</sup>, A.L. Hinson<sup>1,15</sup>, B. Bergamaschi<sup>6</sup>, J.S. King<sup>16</sup>

<sup>1</sup>Dept. of Ecosystem Science and Management, Texas A&M University

<sup>2</sup>Marine Biological Laboratory, Woods Hole

<sup>3</sup>Elder Research, Charlottesville, Virginia

<sup>4</sup>Dept. of Meteorology and Atmospheric Science, Pennsylvania State University

<sup>5</sup>Department of Plant and Soil Sciences, University of Delaware, Newark, DE

<sup>6</sup>United States Geological Survey, Water Mission Area, Menlo Park

This article has been accepted for publication and undergone full peer review but has not been through the copyediting, typesetting, pagination and proofreading process which may lead to differences between this version and the Version of Record. Please cite this article as doi: 10.1029/2019GB006349

<sup>7</sup>United States Geological Survey, Woods Hole

<sup>8</sup>United States Geological Survey, Wetland and Aquatic Research Center, Lafayette

<sup>9</sup>Atmospheric Biogeosciences, The University of Georgia

<sup>10</sup>Dept. of Geography, University of British Columbia

<sup>11</sup>Dept. of Biological Sciences, Rutgers University, Newark, NJ

<sup>12</sup>Dept. of Geological Sciences, University of Florida

<sup>13</sup>Dept. of Earth and Planetary Sciences, Washington University in St. Louis

<sup>14</sup>Faculty of Resource Science and Technology, Universiti Malaysia Sarawak, Malaysia

<sup>15</sup>Dept. of Microbiology, University of Tennessee, Knoxville

<sup>16</sup>Dept. of Forestry and Environmental Resources, North Carolina State University

Corresponding author: Dr. Rusty A. Feagin (feaginr@tamu.edu)

### Key Points

- We created the Blue Carbon (BC) model, which mapped the Gross Primary Production (GPP) of all tidal wetlands within the continental US
- The BC model provides maps of tidal wetland GPP at sub-250 m scales and at 16-day intervals for the years 2000-2019
- The average daily GPP per m<sup>2</sup> was  $4.32 \pm 2.45$  g C/m<sup>2</sup>/day, and the total annual GPP for the continental US was  $39.65 \pm 0.89$  Tg C/yr

## Abstract

We mapped tidal wetland gross primary production (GPP) with unprecedented detail for multiple wetland types across the continental United States (CONUS) at 16-day intervals for the years 2000-2019. To accomplish this task, we developed the spatially-explicit Blue Carbon (BC) model, which combined tidal wetland cover and field-based eddy covariance (EC) tower data into a single Bayesian framework, and used a super computer network and remote sensing imagery (MODIS EVI). We found a strong fit between the BC model and EC data from ten different towers ( $r^2=0.83$ ,  $p<0.001$ , RMSE=1.22 g C/m<sup>2</sup>/day, average error was 7% with a mean bias of nearly zero). When compared with NASA's MOD17 GPP product, which uses a generalized terrestrial algorithm, the BC model reduced error by approximately half (MOD17 had  $r^2=0.45$ ,  $p<0.001$ , RMSE of 3.38 g C/m<sup>2</sup>/day, average error of 15%). The BC model also included mixed pixels in areas not covered by MOD17, which comprised approximately 16.8% of CONUS tidal wetland GPP. Results showed that across CONUS between 2000 and 2019, the average daily GPP per m<sup>2</sup> was  $4.32 \pm 2.45$  g C/m<sup>2</sup>/day. The total annual GPP for the CONUS was  $39.65 \pm 0.89$  Tg C/yr. GPP for the Gulf Coast was nearly double that of the Atlantic and Pacific Coasts combined. Louisiana alone accounted for  $15.78 \pm 0.75$  Tg C/yr, with its Atchafalaya/Vermillion Bay basin at  $4.72 \pm 0.14$  Tg C/yr. The BC model provides a robust platform for integrating data from disparate sources and exploring regional trends in GPP across tidal wetlands.

## 1. Introduction

Tidal wetlands are a critical component of global climate regulation. Producers (primarily plant communities) in these ecosystems acquire carbon dioxide (CO<sub>2</sub>) from the atmosphere and assimilate the carbon into organic tissues (Taiz & Zeiger 2002). The assimilated carbon in these ecosystems is often referred to as 'blue carbon', as it is oceanic- or wetland-related (McLeod et al. 2011; Lovelock and Duarte 2018; Windham-Myers et al. 2018, and references therein). A rough estimate is that these ecosystems may offset between 0.9% to 2.6% of total anthropogenic CO<sub>2</sub> emissions globally (Murray et al. 2011).

After first undergoing respiration and decomposition (Hopkinson et al. 2012; Bond-Lamberty et al. 2018), a portion of this producer-assimilated carbon is then sequestered into deep soil horizons (Chmura et al. 2003, 2013; Duarte et al. 2005) along with allochthonous sources (Bianchi et al. 1999, 2011, 2019). With continuous accretion of this material over time, soil carbon storage rates in some tidal wetlands are estimated to be 50 times greater than rainforests of a similar area, where the forest carbon storage occurs largely aboveground (Bridgman et al. 2006; Nelleman et al. 2009). To properly assess regional and continental United States (CONUS) carbon budgets and their blue carbon potential (Hayes et al 2018), the atmospheric CO<sub>2</sub> assimilation by tidal wetlands must be more accurately quantified.

The Gross Primary Production (GPP) of a tidal wetland represents the total photosynthetic flux of CO<sub>2</sub> between the atmosphere and the surface on a per land area basis before any respiratory fluxes back to the atmosphere are removed. This flux can be empirically modelled from direct site-specific eddy covariance (EC) measurements that record the Net Ecosystem Exchange (NEE) of CO<sub>2</sub>, and GPP can be estimated from these measurements (Reichstein et al. 2005; Lasslop et al. 2010). Conceptually, one way to estimate GPP is to find the difference of ecosystem respiration ( $R_E$ ) from measured NEE as:

$$GPP = -NEE + R_E \quad \text{Eq. 1}$$

While EC measurements provide invaluable information for measuring GPP and understanding functioning of an ecosystem, their spatial representation is limited from a few hundred meters to several kilometers. If we assume that the response functions observed in EC datasets are representative of larger landscapes, we can use those functions in spatial models to map GPP over broader spatial and temporal scales. Several radiation-based models have been based on the conceptual logic of light use efficiency (LUE, e.g., Monteith 1972), which suggests that GPP can be quantified as a function of how plants intercept and convert solar radiation into biomass, within the context of other climatic variables such as temperature and water availability. The most basic elements of the GPP relationship include:

$$GPP = \varepsilon * iPAR * fPAR \quad \text{Eq. 2}$$

where  $iPAR$  is the incident photosynthetically active radiation (PAR) that arrives above the plant canopy,  $fPAR$  is the PAR fraction intercepted by plant leaf surfaces (often modelled as a function of vegetation indices), and  $\varepsilon$  is a multiplicative LUE coefficient that determines the efficiency of converting light photons into biomass for a given plant type. The automated framework of Heinsch et al. (2003, 2006), Running et al. (2004), and Zhao et al. (2005) set the groundwork for mapping GPP at global scales using this basic formula with NASA's Moderate Resolution Imaging Spectroradiometer (MODIS) imagery providing the  $fPAR$  input (for example, producing NASA's MOD17 as a GPP output product at 500 m or 1 km resolution).

While NASA's MOD17 product estimates GPP in some areas occupied by tidal wetlands, it suffers from several limitations, including: (1)  $\varepsilon$  and  $fPAR$  are not specific for tidal wetland plants. Tidal wetlands are either classified as 'water' or designated as a terrestrial ecosystem, though they may act differently (Rocha and Goulden 2009). For example, water inundation can affect both  $CO_2$  exchange (Kathilankal et al. 2008; Malone et al. 2013, Forbrich & Giblin 2015; Zhao et al. 2019) and surface reflectance in short-vegetation wetlands, which is used to estimate vegetation indices and thus  $fPAR$  (O'Connell et al. 2017); (2)  $iPAR$  is derived using older meteorological products interpolated to relatively coarse resolutions (such as National Centers for Environmental Prediction (NCEP) II reanalysis), and moreover these do not incorporate sea-based weather station and buoy meteorological measurements that would be useful along coastal areas (Saha et al. 2014); and (3) the majority of tidal wetlands are distributed in narrow strips along the coastal boundary (Hardisky et al. 1986; Klemas 2011) at scales much finer than the resolution of the land cover classification algorithm/layer used by MOD17. This problem results in  $fPAR$  values that are mixed among multiple terrestrial plant cover types, yielding mixed GPP values, or alternately providing no GPP values in areas incorrectly classified as water.

The overgeneralization of  $\varepsilon$  can be resolved by creating a set of equations that better describe LUE for tidal wetlands. In particular, Barr et al. (2013) used a Bayesian framework that described LUE as a function of temperature, light saturation, salinity and calibrated  $fPAR$  values using the Enhanced Vegetation Index (EVI) band of MODIS. Similar LUE models have been created for individual EC tower sites, often using calibrated Normalized Difference Vegetation Index (NDVI) or other similar metrics for  $fPAR$  (Ghosh et al. 2016; Schile et al. 2013). Still other LUE models have taken into account salinity (Heinsch et al. 2004) or tidal inundation (Kathilankal et al. 2008; O'Connell et al. 2017; Tao et al. 2018). The uniqueness of the Barr et al. (2013) approach lies in the optimization of the LUE inputs that combine to define  $\varepsilon$  through the use of Bayesian statistics. This procedure makes it more suitable for a large-scale extrapolation. Still, no other method has combined this statistical approach with the flexibility to model GPP across other plant physiological types at both a fine spatial resolution and across the large spatial extent occupied by tidal wetland vegetation.

Our overall objective was to model tidal wetland GPP at 250 m scale, while also accounting for wetlands smaller than this area, across the entire CONUS. We quantified GPP and created maps at 16-day averages for the years 2000-2019. To accomplish this task, we built the Blue Carbon (BC) model, which modeled GPP in a spatially-explicit environment. The model was parameterized in a Bayesian framework using tidal wetland cover and EC tower data across a wide range of sites, and then was validated by comparing its output with additional EC tower data sets. Finally, we compared its output against NASA's MOD17 products and other GPP estimates from the literature, and summarized key findings about GPP distribution.

## 2. Methods

### 2.1 BC model overview

We built the Blue Carbon (BC) model using Google Earth Engine (Gorelick et al. 2017). To compute estimates of tidal wetland GPP at a given location and date, our approach with the BC model required an input for each of the variables outlined in Eq. 2. The model approach applied seven basic steps, resulting in GPP spatial map output and comparisons with other products (Fig. 1):

First, specific types of wetlands were defined based on mapping data and EC-tower data availability (Section 2.2).

Second, for modeling LUE,  $\epsilon$  required extensive parameterization within a hierarchical Bayesian statistical framework (Section 2.3). This framework required us to develop LUE equations specific to tidal wetlands, and then find the optimal values of a set of characteristics that quantify the controls of light and temperature on EC-derived GPP. This framework used EC tower datasets at several wetland sites, with datasets spanning multiple years across all seasons (and thus the full range of possible light and temperature controls).

Third, using the results from the Bayesian framework as the BC model inputs, the BC model then calculated Eq. 2 (Section 2.4). The  $iPAR$  inputs were derived from meteorological datasets. The  $fPAR$  inputs were derived from MODIS EVI datasets (MOD13Q1) at 16-day time intervals and at 250 m spatial resolution across the continental US.

Fourth, we developed a unique spatial algorithm to solve the problem of 'mixed pixels' (Section 2.5).

Fifth, we assessed the validity of the BC model by comparing its GPP predictions with field-derived EC tower GPP (Section 2.6).

Sixth, we mapped tidal wetland GPP over the relevant spatio-temporal extent and summarized the results statistically (Section 2.7).

Finally, we compared the BC model with NASA's MOD17 product (Section 2.8).

### 2.2 Tidal wetland classes: Maps and flux data availability and processing

We first identified the location of all tidal wetlands in CONUS and grouped them into four separate classes: (1) woody mangroves, (2) woody freshwater swamps, (3) herbaceous salt marshes, and (4) herbaceous freshwater wetlands. These four classes form a full factorial that includes all tidal wetlands. Our resulting high-resolution, vector-based dataset was composed of polygonal delineations. Hinson et al. (2017) contains more details on the underlying dataset (downloadable from [bluecarbon.tamu.edu](http://bluecarbon.tamu.edu)), which is itself a refinement of the National Wetlands Inventory (NWI) and as such its classification is based on the Cowardin

system (Cowardin et al. 1979). In short, the definition of a tidal wetland in this dataset is based on hydrologic considerations which are listed as specific modifiers (for example, semi-permanently flooded tidal freshwater wetland; Federal Geographic Data Committee 2013).

We then overlaid a MODIS grid on top of this vector dataset and found the area of each tidal wetland class within a 250 m pixel size. This step allowed us to identify the class-affiliation and the percent of each pixel occupied by each class, at the 250 m scale.

Using typical wetlands at sites that represented these tidal wetland types (Table 1), atmospheric fluxes of NEE were determined using the eddy covariance technique (Baldocchi et al. 1988; Heilman et al. 1999). The calculated fluxes were either downloaded directly from Ameriflux or provided by site Principal Investigators (PIs). With the exception of US-NC4, all sites experienced tidal hydrology (the hydrology of US-NC4 is classified as ‘seasonally flooded’ in NWI). In the absence of Ameriflux data associated with tidal freshwater environments, we approximated these classes with EC datasets representing similar species structure. Specifically, we used US-NC4 as a woody freshwater swamp class, but also US-SRR as a herbaceous freshwater wetland class despite its higher salinity range (channel salinity of < 2-10 ppt, e.g., Knox et al 2018; tidal freshwater typically refers to < 2 ppt).

NEE fluxes were first filtered for periods of instrument malfunctioning, insufficient turbulence (Foken et al. 2004, class 0,1), and outliers, as described in Papale et al. (2006). They were next partitioned into GPP and  $R_E$ , following Eq. 2. While nighttime  $R_E$  was detected directly by the EC technique, daytime  $R_E$  was entangled with GPP, requiring the choice of a partitioning algorithm. We used the nighttime partitioning approach by Reichstein et al. (2005) as implemented in REddyProc (Wutzler et al. 2018) to estimate GPP. We review the implications of this choice in the Discussion section below.

## 2.3 Bayesian Framework for Light Use Efficiency

The Bayesian framework was developed to statistically quantify the efficiency of a given tidal wetland plant to convert light photons into biomass. The goal was to quantify the relevant biophysical relationships that underlie Eq. 2 and develop ‘look-up tables’ for each unique wetland class that could be used later by the BC model. The basic concept of our Bayesian framework was to identify the prior probability distribution of values for a given set of parameters (light and temperature conditions) that were most likely to have resulted in a known posterior distribution (GPP values from field-based EC tower datasets). The code was developed in Matlab and WinBUGS (code available on [bluecarbon.tamu.edu](http://bluecarbon.tamu.edu)).

### 2.3.1 Biophysical Relationships

From Eq. 2, LUE can be determined as follows (Barr et al. 2013):

$$\frac{GPP}{iPAR} = \varepsilon * fPAR \quad \text{Eq. 3}$$

Contrary to other approaches,  $fPAR$  was incorporated into the fitting and we utilize  $\frac{GPP}{iPAR}$  instead of  $\frac{GPP}{APAR}$  as the target (where  $APAR$  is absorbed PAR), which limits the number of assumptions that must be made and reduces uncertainty. The purpose of this approach was to match the  $fPAR$  data stream that the BC model will have available to it, as described in sections below.

The mathematical form of the LUE equations and their key input parameters ( $\varepsilon_0$ ,  $T_{min}$ ,  $T_{max}$ ,  $T_{opt}$ ,  $m_{PAR}$ , and  $m_{EVI}$ ) were defined as follows, with a more detailed explanation and rationale for model structure provided in Barr et al. (2013):

$$\varepsilon = \varepsilon_0 * f_{temperature} * f_{saturation} \quad \text{Eq. 4}$$

where  $\varepsilon_0$  is the maximum LUE value under optimum growing conditions, and

$$f_{temperature} = \frac{(T_a - T_{min}) * (T_a - T_{max})}{[(T_a - T_{min}) * (T_a - T_{max})] - (T_a - T_{opt})^2} \quad \text{Eq. 5}$$

where  $T_a$  is the temperature at a given location and time,  $T_{min}$ ,  $T_{max}$ , and  $T_{opt}$  are the minimum, maximum, and optimal temperatures at which the plant type converts light into biomass; and

$$f_{saturation} = 1 - m_{PAR} * PAR \quad \text{Eq. 6}$$

where  $m_{PAR}$  describes the rate at which the plant class's ability to convert energy into biomass saturates as the light intensity increases. This parameter was used by Barr et al. (2013) because they observed a decrease in LUE with increase in PAR in woody plants, but this behavior also occurs in herbaceous plants as well (Kathilankal et al. 2008). In addition,

$$f_{PAR} = 1 - e^{(-m_{EVI} * EVI)} \quad \text{Eq. 7}$$

where  $m_{EVI}$  details how EVI values increase as a function of the plant type's canopy structure. This parameter is valuable particularly in the case of a woody ecosystem, such as mangroves or woody freshwater swamps, as it provides a fit between the apparent reflectance of the canopy surfaces seen at nadir and the actual quantity of photosynthetic surfaces throughout the vertical structure. This improves the accuracy of EVI as a predictor of changes in leaf area in tropical or forested regions, as compared with NDVI (Barr et al. 2012). In testing, we found that it improved the fit for herbaceous plants as well, though not as greatly as for woody. Eq. 7 has the desired properties of being constrained between 0 and 1 such that the fraction of PAR absorbed by vegetation cannot exceed 100%.

### 2.3.2. Look-up tables

Look-up tables were produced by finding the optimal fit for the key input parameters ( $\varepsilon_0$ ,  $T_{min}$ ,  $T_{max}$ ,  $T_{opt}$ ,  $m_{PAR}$ , and  $m_{EVI}$ ) that fed into Eq. 3-7 to predict the posterior distribution of GPP. Four EC tower sites (Table 1) were used for parameterizing the Bayesian framework and producing look-up tables: US-SKR (representing mangroves), US-NC4 (woody freshwater swamps), US-PHM (salt marshes), and US-SRR (herbaceous freshwater wetlands). All other tower sites were not used at this stage of our work. The data from each of these four sites were segregated into parameterization versus validation datasets (Table 1). Once a look-up table was parameterized using several years of data, we validated it using the data from other years.

Performance of the look-up tables was evaluated using the linear relationship between field-derived GPP from the tower sites and that modelled by the Bayesian framework (slope and intercept), the coefficient of determination ( $r^2$ ), and the root mean square error (RMSE). It is important to note that at this stage of the framework, the Bayesian approach utilized the EC tower-recorded  $iPAR$  and temperature records as inputs to the equations (as opposed to the BC model described below, which used remotely-sensed or modelled inputs for these parameters). To find the best look-up tables for later use by the BC model, we tested:

(1) Using two tidal wetland classes (woody, herbaceous) versus the four wetland classes

This test involved grouping the four classes into only two: woody (to include both woody mangroves and woody freshwater swamps) versus herbaceous (to include both herbaceous salt marshes and herbaceous freshwater wetlands). For each tower site in the four-class test, we randomly excluded one year of data for validation; the rest was used for parameterization. For the two-class set up, we randomly excluded two years of data for validation; the rest was used for parameterization. The reason behind this difference was that when grouping into two classes, there are more available data in each class and therefore more records are saved for validation while maintaining statistical robustness during parameterization.

We found that the two-class woody-vs-herbaceous parameterization was more efficient and parsimonious than using the four wetland classes (Table 2). For both the woody and herbaceous class, the statistical fit and errors were approximately halfway between those of the more specific classes that comprised each group when they were run separately. This result suggests the appropriateness of grouping tidal wetlands based on similarities in anatomy. Further reasoning for using the two-class woody-vs-herbaceous grouping is that the sample size increased for both parameterization and validation datasets, and the fact that more of the additional ‘offsite’ validation datasets also became applicable to each grouping (as described in sections further below).

We also tested groupings based on sub-tropical (US-SKR) versus temperate (US-SRR, US-PHM, US-NC4) wetlands, mixed across anatomical categories, but the statistical relationships were weaker; in this case, the temperate group performed roughly similar in  $r^2$  to its three constituent class sites, but the sub-tropical group matched the lower  $r^2$  values shown for this mangrove site in Table 2 (~0.65) as US-SKR was the only representative. The greatest uncertainty in LUE among all combinations of sites and classes was for the mangrove class, which was interesting given that the Bayesian approach has been refined by both the present study and Barr et al. (2013), and in addition this site has the largest number of observations among all EC tower sites. The fact that US-SKR was consistently lower in  $r^2$  suggests that tropical wetlands outside of the CONUS and outside the scope of this study, with still more consistent green leaf cover year-round, could prove even more difficult to model for GPP.

(2) Including a light saturation coefficient in the look-up tables.

We tested for and found a large benefit to quantifying the effect of light saturation in woody canopies, particularly for mangroves, when including the  $m_{PAR}$  parameter (Table 2). Canopy light saturation to photosynthesis was not strongly observable in any herbaceous class or group, though including this parameter slightly increased the  $r^2$  values. To maintain consistency of the table structure across groupings, and to protect against the possibility that light saturation could still occur at unparameterized sites (neither of the parameterized sites US-SRR and US-PHM are in the southern part of the US, where there is consistently higher PAR), we decided to move forward with using the  $m_{PAR}$  parameter for all classes.

(3) Using the median of the distribution from the look-up table

When investigating the distribution of  $\varepsilon_0$ , we found it to be skewed to the right. Moreover, we found that the performance of the tables increased when using the median value of the Bayesian-derived distribution for the other parameters as well, as opposed to using the mean for these parameters; this was particularly true for the mangrove cover class and accordingly, the woody grouping (Table 3). We thus chose to move forward with the median look-up table values, as was done in Barr et al. (2013).



#### (4) Excluding salinity and tidal inundation

Salinity and tidal inundation depth were not included as parameters in the final framework, though we tested and constrained their potential contribution to improving accuracy. Both of these variables vary at fine spatial and temporal scales, complicating their inclusion. For example, inundation frequency and duration were different for each site, depending on site elevation, vegetation height and tidal amplitude, and they cycled at higher frequencies than the 16 days of constraining MODIS datasets. Similarly, salinity can spatially vary greatly over a few meters and fluctuate quickly with rainfall or the tidal cycle. No standardized approach has been developed to partition the contribution of these variables to NEE fluxes in tidal wetlands, and no input streams currently exist that can provide mapped inundation or salinity at the scale of the other parameters, at least for a manner applicable across broad spatial scales.

To estimate the effect of salinity and the error induced by excluding it from the BC model, we assessed the differences in the parameterization at the US-SKR site (Barr et al. 2013) and the US-PHM site (Forbrich et al. 2018). We found no added measurable benefit to including salinity into the framework when predicting GPP (Table 3, only US-SKR data shown). This finding was somewhat surprising, and led us to ask why excluding it did not make an important difference, which we review further in the Discussion section below.

#### 2.4 Running the BC Model

To calculate  $\varepsilon$  in Eq. 3, across all tidal wetlands in the CONUS, the BC model used the final optimized look-up table values (Table 4). The optimal LUE model defined only two tidal wetland classes (woody, herbaceous), used the median values from the Bayesian-derived distribution and fed them into Eqs. 3-7. These two classes were quite similar in  $m_{EVI}$  and temperature-related variables, though the LUE coefficient  $\varepsilon_0$  varied greatly. This result emphasizes that the primary difference among the woody and herbaceous classes was LUE; this is of benefit for modelers because there is relatively high confidence in the ability to delineate woody versus herbaceous plant cover using imagery (as opposed to lower confidence in the case of the four-class parameterization, where one must sort various classes based on salinity which can be more difficult to map).

For  $iPAR$  in Eq. 3, we used the NCEP Climate Forecast System Version 2 6-hourly products (CFSV2). These products were created in 2011 and contain improvements on the NCEP Reanalysis II products used by MOD17 and Barr et al. (2013). These improvements are primarily due to the integration of terrestrial and marine datasets (Saha et al. 2014). We obtained the downward solar radiation flux at 6 hour intervals (imagery layer name in Google Earth Engine: Downward\_Short-Wave\_Radiation\_Flux\_surface\_6\_Hour\_Average), summed them for each 24 hour period and divided by 4, and then found the proportion that is available in the visible portion of the spectrum as PAR (\*0.45) to obtain the daily light integral in Watts  $m^{-2}$ , and finally converted values into units of  $mol\ m^{-2}\ d^{-1}$  (\*4.57\*10<sup>6</sup>\*86400). We also obtained the temperature at 2 m of height above the ground for each day (Temperature\_height\_above\_ground). The CFSV2 dataset inputs were then interpolated to match the grain size of the imagery discussed below, following methods similar to Zhao and Running (2005).

To find  $fPAR$  in Eq. 3, which is specific to each location and time across the CONUS, we chose the EVI band of the MOD13Q1 16-day MODIS-satellite product as this was available at 250 m resolution (Didan et al. 2015), and thus was best able to resolve relatively fine-scale wetlands. Following Zhang and Running (2005), we identified the pixels that were obscured

by clouds, smoke, or ice using the Pixel Reliability band. We then removed those pixels and gap-filled them by using the average of values from the preceding and following dates. Some areas of wetlands fell outside of the MOD13Q1 extent, due to usage of the MODIS water mask product upstream in NASA's MODIS processing suite of products. We noted that this phenomenon appeared to be primarily limited to the southern Atlantic Coast wetlands, such as in Georgia or South Carolina, and varied with time in the MOD13Q1 product, in that a single pixel would be included for almost all imagery dates, and yet would drop out on a particular date. In these cases, we resolved this issue using the approach described below in the section on pixel purity. Similarly, the MOD13Q1 product can present abnormally low or high EVI for a pixel, presumably because of abnormal reflectance from the ground, or from sensor or algorithmic error, captured by the upstream NASA product MOD09Q1 and then inherited by MOD13Q1. In these cases, the abnormal values are constrained and minimized by the functional limits provided by Eq. 7 for  $fPAR$ .

## 2.5 Pixel Purity and Spatial Interpolation

Tidal wetlands are often linear in their areal geometry, arranged parallel to the coast, and many are smaller than a single 250 m pixel. The result is that a pixel can be spectrally-mixed, with multiple plant or land cover types interspersed with one another. For example, within a single 250 m pixel, there could be a small wetland, a road, some cropland, and some impervious surface. To correctly calculate GPP, one would prefer that this pixel be homogeneous because each of the cover types has a different set of biophysical responses for Eqs. 3-7. One approach is to exclusively use homogeneous pixels, but this would not capture the majority of the tidal wetland areas within the US. The disadvantage to calculating GPP in mixed pixels is that one degrades the accuracy of the estimate, while the disadvantage to using only homogenous pixels is that one loses the ability to account for the total GPP across all wetlands.

To address this challenge, the BC model was optimized at a level of 'pixel purity' for which these two competing interests were balanced. Pixel purity is defined as the percent of a pixel that was covered by a given tidal wetland class (accomplished by overlaying the 250 m MODIS footprint with the vector-based Hinson et al. (2017) dataset described earlier). All work on the pixel purity portion of the BC model was performed for the two classes separately, woody and herbaceous. At a later stage as described below, the resulting GPP from the entire procedure was combined for the two classes based on their proportional coverage within each pixel.

We found the optimal pixel purity level to be greater than or equal to 80%. We then ran the BC model to find GPP using only those pixels that exceeded the purity test ( $\geq 80\%$ ), and then spatially interpolated the GPP results across the remaining pixels of similar class ( $< 80\%$ ). The purpose was to optimize the accuracy of the GPP estimate using high quality tidal wetland pixels, and transfer these values across distance to lower quality pixels, while also not overextending the ability of those transfers to be valid. The Inverse Distance Weighted (IDW) method was used with a power of 2, to minimize the required assumptions (Issaks and Srivastava 1989). However, before finally settling on the 80% threshold, we performed several tests across multiple levels of purity (every 10% from 0 to 100), and estimated the assumptions and errors of each. These tests sought to identify:

- (1) The spatial distances across which interpolation could optimize the GPP while minimizing errors

Our primary goal here was to obtain quality estimates of GPP from relatively pure tidal wetland pixels and interpolate those values into mixed-class pixels that contain smaller fractions of wetlands. However, we also wanted to know the cost in terms of accuracy of conducting this interpolation. For the woody and herbaceous classes separately, we used semi-variograms to quantify the spatial variability of GPP across distance. A semi-variogram is a geostatistical tool often used to identify spatial autocorrelation, to test Tobler's law of geography that 'things that are closer together are more related than things that are farther apart', or to detail the spatial structure of variance (Issaks and Srivastava 1989). In this instance, a semi-variogram can clarify the distances over which interpolation is most valid, and the mean error induced by conducting the interpolation. The standard equation is:

$$\hat{\gamma}(h) = \frac{1}{2|N(h)|} \sum_{(i,j) \in N(h)} |z_i - z_j|^2 \quad \text{Eq. 8}$$

where  $\hat{\gamma}$  is the semi-variance at scale bin  $h$ ,  $z$  denotes the GPP value for two points in a pair of points  $i$  and  $j$  that are separated by a distance that falls within scale bin  $h$ , and  $N(h)$  is the number of all possible pairs within  $h$ . For a given scale of inquiry, Eq. 8 finds the squared differences between all paired values and standardizes them by the number of pairs times two; this provides a measure of dataset variance at multiple spatial scales. We performed this analysis using all pixels for July 12, 2018 across CONUS, as this time of year coincided with the average annual peak in GPP at a national scale and would provide the greatest amount of variance in the dataset.

We found that the woody class was the limiting class, with a minimum semi-variogram range at ~12 km and a secondary range at ~65 km (Fig. 2a). From here forward for all subsequent tests, we only describe the woody class test results at the 80% threshold and on the July 12, 2018 date. Interpolating GPP from the  $\geq 80\%$  pixels to the  $< 80\%$  pixels across distances less than 12 km provides ~3 times more accurate results than randomly drawing a GPP value from the  $\geq 80\%$  pixels (sill of ~0.012 is ~3 times larger than nugget of ~0.004). At distances greater than 12 km but less than 65 km, the interpolation provides ~2 times more accurate results (sill of ~0.020 and nugget at 12 km of ~0.012).

It is important to point out that even if an interpolation were to occur across distances greater than 65 km, the GPP value would still be constructed and arrive from pixels that were  $\geq 80\%$  tidal wetland. This situation would be far preferable to using a GPP estimate when the majority of the area of the pixel was of a non-tidal wetland class (for example, incorrectly assuming the GPP is a valid prediction when in fact the majority of the pixel is of water or an urban area).

## (2) The distribution of the low purity pixels as a function of distance from high purity pixels

The large majority of low purity pixels are within a relatively close distance to high purity pixels (Fig. 2b), suggesting that in most cases interpolation only need to occur across short distances. For example, in the case of the woody class using the 80% threshold, over 89% of the  $< 80\%$  pixels had a nearest neighbor  $\geq 80\%$  pixel of less than 12 km. Over 98% had a nearest neighbor of less than 65 km. Moreover, the few pixels that were forced to accept interpolated values from a relatively far distance, were quite low in their percent cover of tidal wetlands (Fig 2b); in other words, the total quantity of GPP at a national scale that had to be interpolated over distances greater than the secondary range of confidence (~65 km) was quite small.

## (3) The relative correction in GPP afforded by interpolation

For pixels  $<80\%$  purity, the nearest neighbor that is  $\geq 80\%$  often has a relatively higher GPP in most cases (Fig. 2c). In some pixels with  $<80\%$  purity, there are some abnormally high GPP estimates as compared with their nearest neighbor that is of higher purity (circles on the upper left side of the 1:1 line and those on the far left side in Fig. 2c; interpolation would presumably correct these overestimates. Other  $<80\%$  purity pixels appear abnormally low (circles on the lower right side of the 1:1 line and along the bottom of the graphic in Fig. 2c), though in these cases we cannot discern whether this relatively lower value is due to the percent cover of the wetlands also being lower or the actual GPP estimate itself.

We next sought to identify the extent to which the final interpolated product improved the GPP estimates. Because there were no additional validation datasets available outside of the ten EC tower sites, and relatively few of those sites resided in pixels with  $<80\%$  purity, we had to develop an alternative method to quantify the effect of the interpolation on relatively isolated or low purity pixels. Thus, we removed all GPP predictions by the BC model within a 12 km buffer of the latitude and longitude of each of the ten tower sites (as noted above, 12 km was the limiting distance for the woody class to obtain benefit from interpolation, wherein we obtained a three-times better estimate than a random draw from the rest of the  $\geq 80\%$  GPP dataset greater than this distance). After removing all pixels within 12 km, we then re-implemented the 80% threshold interpolation procedure.

Whether spatial interpolation was performed by the BC model in the standard case, or performed after removing all pixels within 12 km of each EC tower site, the predicted GPP by class was multiplied by the percent cover of each class in the pixel for the woody and herbaceous classes separately, and then the two were summed to find the GPP in each pixel.

## 2.6 Validation

The BC model output was validated by comparing its predicted GPP with field-derived GPP from the ten EC tower sites (Table 1). For four of the tower locations, some years were used during parameterization of the Bayesian model (designated ‘P’ in Table 1), while other years were used for validation (designated ‘V’ and ‘N’). For the other six ‘offsite’ locations, all data was used only at the validation stage (designated ‘O’). The BC model performance was evaluated using linear regression and standard metrics for goodness-of-fit.

This comparison occurred using a single BC model pixel that covered the latitude and longitude position of the EC tower. We tested the effect of using multi-pixel footprints and at distances varying from 250 to 50,000 m in radius, using the US-SKR site as a test case. To generalize, the cost was spatial accuracy when using a larger number of pixels across a wide radius and averaging the GPP values for comparison, but the benefit was to smooth temporal spikes or slight errors by leveraging the power of a larger set of pixels from which to obtain the estimate. However, the true differences among the various tests was quite small. Based on these tests, we used the single pixel approach as it was the most parsimonious.

## 2.7 Summaries of GPP

After validation of the BC model, GPP was mapped across the CONUS at 16-day intervals for the years 2000-2019. Daily average per  $\text{m}^2$  GPP and total annual GPP were calculated within individual tidal wetland pixels, across the entire CONUS.

In addition, the quantities within the tidal wetland pixels were summarized for three oceanic coasts (Gulf of Mexico, East Atlantic, West Pacific), individual states, and for 291 estuaries (EDAs) and coastal drainages (CDAs) in NOAA’s Coastal Assessment Framework (CAF;

NOAA 2018). The daily average per m<sup>2</sup> GPP was derived by averaging all of the tidal wetlands' pixel values contained within the given area of a coast/state/EDA/CDA, whereas the total annual GPP quantity was found by summing all of these values in the given area.

Importantly, the values reported for a geographic unit are not averaged relative to the *total* area of each unit, but rather only for the *tidal wetlands area* within each unit. Further, the extrapolation of pixel values across the geographic unit plays no part in this process. As an example, if the average tidal wetland GPP in a given state was reported as 5 g C/m<sup>2</sup>/day, this was simply the average for the tidal wetlands that were found within the state. The same procedure applies to the sum of GPP - the GPP sum is *not* extrapolated to the unit extent under an assumption that all of the area within the unit would be tidal wetlands – rather, the value is simply the sum of the tidal wetland GPP that exists in the unit. The coasts/states/EDAs/CDAs are solely geographic areas wherein we can talk about the tidal wetlands within them – the entirety of each is not composed of tidal wetlands. We summarized these values and reported statistical quantities such as the means and standard deviations.

## 2.8 Comparison with Other Products

The BC model was compared against the most up-to-date NASA MOD17 GPP product, MOD17A2H.006. The goodness-of-fit between the MOD17 product and the EC tower data was evaluated using linear regression and standard metrics.

## 3. Results

### 3.1 Validation

For validation of the BC model, it made little difference whether the field-derived EC tower data was limited to only the six 'offsite' towers (n=260 unique 16-day periods linearly regressed among all combined sites for  $r^2=0.79$ ,  $p<0.001$ , RMSE=1.23 g C, with average error 19% off true value; group 'O' in Fig. 3a) or included all ten tower sites (n=522,  $r^2=0.83$ ,  $p<0.001$ , RMSE=1.22 g C, average error was 7% off true value; groups 'O', 'V', and 'N' in Fig. 3b). The strong fit in the former case suggested that the BC model described the variance in GPP quite well for new locations. In the latter case, validation data were included from the original four sites, but came from separate years in the record and was not used during parameterization of the Bayesian framework. If the validation effort included all data available to us (even those data used during parameterization of the Bayesian framework, for the purpose of developing the look-up tables that were later used by the BC model – importantly, this data is not equivalent and has differing inputs generating it for the framework versus the model, as described in Section 2.3.2), the result was generally the same (n=692,  $r^2=0.83$ ,  $p<0.001$ , RMSE=1.20 g C, average error was 6% off true value; groups 'O', 'V', 'N', and 'P' in Fig. 3c).

Given the consistent fit between BC modelled and field-derived EC GPP in each instance, the BC model was considered relatively robust across differing tidal wetlands. Still, it was clear that the model captured the behavior of particular class types and tower locations better than others after further inspection of the second case mentioned above (using all validation data only, i.e. 'O', 'V', and 'N'). For the woody class in particular, the model tended to match well at lower levels of GPP, over-predict GPP at moderate levels of GPP, and under-predict at higher levels (Fig. 4a).

The model also performed slightly different for each tower (Fig. 4b, Fig. 5). Most notably, all observations at the US-LA1 tower in Louisiana were over-predicted. If we removed the US-LA1 tower from the dataset, then the  $r^2$  values increased an additional  $\sim 0.05$  and the average error was approximately halved, for each of the statistical tests described above. Several observations at the GCE tower in Georgia and the US-SRR tower in California were over-predicted at their respective higher GPP levels, and observations at US-VFP in Virginia and US-STJ in Delaware (in one year) were under-predicted. The reasons are likely unique in each case. For example, US-LA1 is eroding relatively quickly and US-SRR contains non-wetlands in its footprint depending on wind direction. Or, in the example of US-STJ, the BC model does better in some years than others. An extensive assessment of the specific details for each tower are outside the scope of the present study, but may prove fruitful ground for future study. In sum, the BC model tended to over-predict GPP slightly at high GPP levels yet under-predict GPP slightly at low GPP levels. Still, the slope of the linear regression of the BC modelled versus field-derived EC GPP was relatively close to 1:1 (0.97 slope with intercept of 0.24, using 'O', 'V', and 'N' only), demonstrating low bias in either direction.

When we intentionally removed all pixels within 12 km of an EC tower and interpolated across that distance, the fit decreased ( $n=478$ ,  $r^2=0.76$ ,  $p<0.001$ ,  $RMSE=1.47$ , average error was 7% off true value; using groups 'O', 'V', and 'N' only; Figs. S1-S2). There was a decrease in internal model precision ( $r^2$  decreased) and the magnitude of the difference from the EC tower data was larger ( $RMSE$  increased), but since the dataset was slightly different (the US-NC4 dataset was not included due to a practical issue) the average error was not substantially different. The BC model also over-predicted more strongly in this case (slope of 0.89).

Interpolation also provided an additional correction for CONUS-scale work. While the BC model included all tidal wetlands mapped by Hinson et al. (2017), the MODIS EVI 250 m resolution product did not provide data for all of them. The upstream NASA product MOD09Q1 removed many pixels where there were indeed tidal wetlands, designating them as 'water' in its masking procedure, and this issue was then inherited by MOD13Q1. Approximately 24.5% of the available tidal wetland pixels are incorrectly removed by the NASA MODIS products (often containing the smaller sized wetlands with less average GPP than the rest of the dataset), and this results in a 16.8% under-estimation of GPP at the CONUS scale (in addition to the more general errors introduced by the MOD17 algorithm). We arrived at this value by comparing a summarization of the GPP for the interpolated maps versus the non-interpolated maps. Our interpolation procedure solved this problem by populating these pixels.

### 3.2 Summaries of GPP

The BC model analysis found that between 2000 and 2019, the average daily GPP per  $m^2$  of tidal wetland cover across all CONUS locations and dates was  $4.32 \pm 2.45$  g C / $m^2$ /day (Fig. 6 and 7; values represent the mean  $\pm$  standard deviation among the 16-day periods). The average maximum across all CONUS locations (i.e., the max among 16-day periods, across a given year) was  $7.92 \pm 0.32$  g C / $m^2$ /day, reaching maximum values in June or July every year, except for 2011 when it peaked in late May. The average minimum across all CONUS locations (i.e., the min among 16-day periods, across a given year) was  $1.00 \pm 0.12$  g C / $m^2$ /day, and lowest in late December or early January every year.

The total annual tidal wetland GPP for the entire continental US was  $39.65 \pm 0.89$  Tg/yr (Fig. 8; mean  $\pm$  standard deviation among the years). The total annual GPP for the Gulf, East and

West Coasts was  $25.75 \pm 1.14$ ,  $13.28 \pm 0.64$ , and  $0.62 \pm 0.04$  Tg/yr respectively. The quantity of GPP in the Gulf Coast was nearly double that of the East and West Coasts combined.

The state of Louisiana alone accounted for  $15.78 \pm 0.75$  Tg/yr. Florida was second at  $7.27 \pm 0.24$  Tg/yr. All other CONUS states, excepting Florida, added up to  $16.60 \pm 0.84$  Tg/yr, a value nearly equivalent to Louisiana. In fact in 2004, the estimated total annual GPP in Louisiana alone was more than that for the rest of CONUS excepting Florida. The relatively high quantities for Louisiana and Florida were due to both the large areal coverage of tidal wetlands and higher average daily GPP per  $m^2$  (both can be seen in Fig. 6).

The Atchafalaya/Vermillion Bay estuarine basin had the highest total annual GPP at  $4.72 \pm 0.14$  Tg/yr (Table 5, Fig. 7a) out of the 291 total EDAs/CDAs in NOAA's CAF framework. Ranking these in order going from the highest total annual GPP to the lowest, several other bays in Louisiana, Chesapeake Bay on the US Mid-Atlantic, and the North and South Ten Thousand Islands region in the Florida Everglades also ranked in the top 20. Thirteen of the top 20 on the list were on the Gulf Coast, and the other seven were on the East Coast. The West Coast was not represented until San Francisco Bay, number 35 out of all 291 basins.

### 3.3 Comparison with NASA's MOD17

As compared to NASA's MOD17 GPP product, the BC model provided a better fit to the observed GPP at all tower sites (Fig. 5). The BC model explained the variation in GPP about twice as well as MOD17; the MOD17 fit was relatively weak ( $n=692$ ,  $r^2=0.45$ ,  $p<0.001$ ,  $RMSE=3.38$  g C, and its average error was 15% off true value). The slope of the relationship deviated further from a 1:1 line (0.93) and the model intercept was quite a bit larger (1.02). The MOD17 product exhibited abnormal positive spikes in GPP at several sites, particularly in summer months when GPP was relatively high (Fig. 5). The BC model avoided these spikes, likely because of the functional limits on GPP provided by the  $m_{PAR}$  and  $m_{EVI}$  parameters (MOD17 does not include these parameters). MOD17 occasionally presented abnormally low values, which the BC model avoided as well. The BC model worked much better at the US-SKR woody mangrove site in Florida.

Perhaps most notably, the BC model was able to capture the trend at the GCE herbaceous salt marsh site in Georgia and the US-LA1 herbaceous salt marsh site in Louisiana reasonably well, while the MOD17 model predicted zero GPP due to its lower resolution and inability to adequately resolve the spatial nature of fringing tidal wetlands (NB: Tao et al. 2018 show a MOD17 value for the GCE site, though it is actually acquired from another pixel within the tower footprint that was more homogeneous in wetland cover). These two instances highlight the problems with MOD17 and other products that do not account for mixed pixels or small wetlands.

MOD17 estimated the average daily GPP per  $m^2$  as  $7.96 \pm 3.93$  g C / $m^2$ /day (as compared to  $4.32 \pm 2.45$  by the BC model). However, because it also incorrectly removed 24.5 % of the available tidal wetland pixels, it calculated the total annual GPP for the entire CONUS as  $50.04 \pm 3.94$  Tg/yr (versus  $39.65 \pm 0.89$  Tg/yr for the BC model). In other words, MOD17 appeared to get a somewhat reasonable answer, but only because these two factors counteracted each other numerically. Across each of the metrics that we tested, MOD17 results had much greater variance and mean bias than that of the BC model.

## 4. Discussion

### 4.1 Comparisons with Other Studies

There have been no previous studies that have calculated GPP across all tidal wetlands in the continental US. However, Najjar et al. (2018) found a rough estimate for net uptake by tidal wetlands, for the East Coast and Canadian portions of the Gulf of Maine, to be  $5.3 \pm 1.5$  Tg/yr. The BC model calculated GPP as  $13.28 \pm 0.64$  Tg/yr for ~98% of this tidal wetland area (excluding the Canadian portions). Assuming the difference is due to respiration and lateral flux of dissolved inorganic carbon (DIC) into the water column ( $(13.28 * 0.98) - 5.3 = 7.7$ ), this would require  $R_E$  plus the lateral flux to be on the order of 58% of GPP for this area ( $7.7 / 13.28 = 58\%$ ). Average annual  $R_E$  is likely higher based on our experience, closer to 80% of GPP, and the lateral flux is largely unknown (though some ranges are available in Bianchi et al. (2019)). The difference suggests that the Najjar et al. (2018) value is too high, which could be due to the mass-balance, literature-review approach used in Najjar et al. (2018).

In the future, the BC model output could be compared with aboveground biomass datasets, particularly those using calibration-grade, national level datasets such as Byrd et al. (2018). It could also be compared with belowground carbon burial estimates (see Fig. S3 for an example), made for the purposes of the US National Greenhouse Gas Inventory (Hinson et al. 2017; Crooks et al. 2018; Holmquist et al. 2018). Regional studies could also provide fertile ground for cross-comparison (Ghosh et al. 2016).

Due to the absence of other CONUS-scale GPP studies to compare against, we developed a heuristic calculation. This calculation is essentially a first-order, Tier 1 approach (EPA 2017; Hiraishi et al. 2014), where we assumed that a central value is appropriately representative (e.g., Holmquist et al. 2018). We first found the average GPP from the observed EC tower datasets that we had combined at 16-day intervals, obtaining  $3.80 \text{ g C/m}^2/\text{day}$  ( $n=709$ ), a value below that of the BC model ( $4.32 \text{ g C/m}^2/\text{day}$ ). We then multiplied this average by the total area of the tidal wetlands, or 24,946 to 26,818  $\text{km}^2$ , and the number of days. The first value for area is from Hinson et al. (2017) and is the quantity for all tidal wetlands used by the BC model, and the second is from Windham-Myers (2018), both of which are similar to Bridgham (2007).

This resulting 34.63 to 37.23 Tg/yr was ~10% below that of the BC model value, because the heuristic calculation used the average from ten sites to calculate the GPP alone, and these values were not appropriately area-weighted for CONUS-scale work. For example, 54.6% of CONUS tidal wetlands are in Florida and Louisiana (data from Hinson et al. 2007's Table S2), yet only 26.5% of the EC tower dataset values came from these states. One would have to find a quite large number of EC tower sites to appropriately represent the productivity across areal coverage of CONUS wetlands, in order to begin to make a reasonable heuristic calculation. The BC model eschews the heuristic and extrapolative approach, and rather identifies the unique LUE and GPP response for each pixel independently, only using the EC tower data to build an understanding of LUE through the Bayesian framework. Moreover, the BC model has the advantage of allowing one to visualize the variance in spatial and temporal patterning at finer scales.

Maps of the spatial and temporal variability are required to understand how GPP responds in a changing environmental context (Fig. 9). Stressors such as tropical cyclones, relative sea level rise, freezes, and drought do not occur continuously in space or time. With detail, the BC model can detect the effects of these stressors on tidal wetlands, over a large range of dates. For example, one could explore the effect of tropical cyclones on tidal wetlands using



an ‘economy-of-scale’, ‘big data’ style approach by mapping the changing GPP before and after these storms. Due to the voluminous nature of the final product, GPP for any tidal wetland at 16-day intervals, the BC model products allow scientists to formulate hypotheses and ask new questions in ways that were not formerly possible.

#### 4.2 Optimizing the Choice of Wetland Classes

One direction for BC model improvement is to further optimize the choice of wetland classes. As more EC tower sites become available for and from the research community, the statistical benefit to creating more specific biophysical classes increases. A drawback to our current validation efforts was that we could not validate with ‘offsite’ towers for the woody class, but rather were limited to cross-year validation, though across both herbaceous and woody classes we had six of these ‘offsite’ tower locations. The situation became even more limited when considering the four-class system of woody mangroves, woody freshwater swamps, herbaceous salt marshes, and herbaceous freshwater wetlands. However, at least initially, our results show that the primary behavior of tidal wetlands was adequately captured by herbaceous versus woody categories alone.

The reality is that more towers are required to more finely parse the biophysical classes or to build geographically-dependent classes. In particular, more EC towers are needed in tidal freshwater swamps, as they compose a fair quantity of tidal wetlands and are unique in physiology. Other interesting options include unvegetated and wind tidal-influenced salt flats or salt pans, and mud flats. With more EC tower datasets, C4 grasses and C3 succulents/rushes could be parsed into separate categories. We initially tried to include a succulent class based on *Batis maritima* from an EC tower in Texas, US-TX9, but the dataset was not workable due to a low number of observations.

In terms of geography, the GPP in the three southernmost herbaceous sites (US-VFP in Virginia, GCE in Georgia, and US-LA1 in Louisiana) was not modelled as well as the other herbaceous sites; US-VFP was under-predicted and GCE and US-LA1 were over-predicted (Figs. 4 and 5). The look-up table produced by the Bayesian framework for the herbaceous class was determined based on wetlands from differing climate zones (US-PHM in New England, and US-SRR in California) and parameters like the optimum temperature may not have been well described. However, the fact that one site is under-predicted and the other two over-predicted speaks against physiological constraints as the reason for the mismatch between EC tower data and the BC model. Another possible factor could be the difference in reflectance from the more northern sites versus the more southern sites (Bartlett et al. 1988), such that  $fPAR$  was not well described in southern marshes in our model. We also noticed that the seasonality (in both EVI and GPP) was pronounced in US-PHM and US-SRR, which were used for our parametrization, while the peak values in the southern marshes were lower. Thus, a lower signal to noise ratio in these input variables may lead to a larger uncertainty at these sites.

#### 4.3 Standardizing EC Tower Measurements for Modelling Purposes

It should be pointed out that field-derived EC tower data should not be considered the ‘gold standard’ for validation efforts, as they are not directly empirical. EC tower data is modelled based on empirical measurements. Thus, the variance and error described in the ‘validation’ procedure is not solely due to the BC model. The EC tower measurements and data manipulation also may be responsible.

Although some standardized approaches have been adopted within the EC community, there is still no consensus about the ‘best’ way to measure NEE. The instruments used to measure often vary from one site to the next, and the integrity of the data depends on calibrations, maintenance, and user error. The footprint of each tower can also vary both spatially and temporally with wind speed, direction, and surface properties. Each tower site has a different percent cover of tidal wetland plants, a different mix of additional cover types, and a different degree of spatial heterogeneity among these cover types.

Moreover, the modelling of the measurements taken from a tower are only reliable under a set of predetermined conditions. The choices made by the investigators about how to adjust for more complex conditions can vary for each EC tower site. For example, assumptions can fail during daytime unstable conditions when wind speeds are very low, or during nighttime stable conditions where low or zero turbulent transport occurs but where other processes are often present (e.g., mesoscale contributions, flow meandering). Filtering the data series can remove these types of events, but if then replaced by estimates from windier conditions, the fluxes can be under-estimated. Investigators must decide whether to include or discard data acquired from the times surrounding sunrise and sunset, and they must also decide how to handle data from the back of the tower.

The choice of how to partition NEE is also critical. We chose the partitioning nighttime partitioning approach by Reichstein et al. (2005) as implemented in REddyProc (Wutzler et al. 2018) for all ‘offsite’ locations with the exception of US-HPY (which we obtained already partitioned), but there are other possible approaches. Other methods use light response curves to fit daytime data, and the  $R_E$  can be estimated as the offset (Lasslop et al. 2010). In the future, the overall fit between the EC tower data and BC model could be improved by using such methods since the Bayesian look-up tables are also tuned for LUE. In this sense, the variation due to partitioning the  $R_E$  component likely contributes the greatest uncertainty to our field-derived EC tower GPP (Desai et al. 2008; Wehr et al. 2016).

To extend the BC model to include Net Primary Productivity (NPP), it would be necessary to add an autotrophic respiration module, possibly using a similar framework as for GPP. This would need to be added and then the remaining parameters in Eq. 1 would be spatially modelled, including  $R_E$ ,  $-NEE$ , and Net Primary Productivity (NPP). A standardized approach focusing on the adequate representation of all sources of respiration would be valuable (e.g., Barba et al. 2018; Keenan et al. 2019) and improve both EC tower and BC model datasets.

An integrative approach such as the present study demonstrates the importance of standardizing EC measurements and modelling. Efforts toward such standardization will ultimately benefit the scientific community.

#### 4.4 Improving the Bayesian Framework

Additional variables could also be included into the Bayesian framework. These could include water inundation level similar to O’Connell et al. (2017) or salinity similar to Barr et al. (2013). At least based on the tests that we conducted herein, these parameters are likely to provide minimal improvement, relative to the effort required to create national-level mapping products that could accurately express these values at 16-day temporal resolution.

We found no added measurable benefit to including salinity into the Bayesian framework when predicting GPP (see the section on look-up tables). This finding was somewhat surprising, and led us to ask why excluding it did not make an important difference. A possible explanation is that salinity co-varies with another factor, for example leaf area index

and  $fPAR$ , such that salinity does not add explanatory power to the model. Alternately, the salinity effect is delayed in time beyond the 16-day window used to drive the BC model. At US-SRR, Knox et al. (2018) showed no instantaneous effect of an increase in salinity on daily LUE, and similar findings have been seen at US-STJ. However at US-PHM, US-SRR, US-SKR, and GCE, variation in salinity appears to drive interannual variation in GPP (e.g., Wieski and Pennings 2013). At these sites, EVI varies accordingly between years, with higher values in more productive years.

Tidal inundation can result in the lateral export of dissolved inorganic carbon (DIC) into the water column (Wang et al. 2018), thereby suppressing the full estimate of  $R_E$  when using EC measurement methods alone (Knox et al. 2018). This situation creates uncertainty in a GPP estimate. For example, Troxler et al. (2015) report an increase in  $pCO_2$  concentrations in the flood water in a mangrove forest, indicating on-going respiration under submergence. These studies highlight the need to incorporate DIC flux estimates into both the carbon budget and partitioning approaches. In herbaceous salt marshes that experience little tidal inundation, the observed suppression is reported to be small (Artigas et al. 2014; Forbrich & Giblin 2015; Schaefer et al. 2019), but this may not be the case for fully tidal systems or different plant classes. Although no standardized approach currently exists, an incorporation of this lateral flux could improve our ability to model carbon fluxes.

Even though the BC model did not utilize tidal inundation or salinity datasets, it provided a better or similar fit to the observed EC flux tower data than studies that did at specific locations. For example, for the GCE site only, Tao et al. (2018) obtained an  $r^2 = \sim 0.46$  and RMSE of  $\sim 20\%$  of the range. Their tide-corrected MODIS data set marginally improved the statistical model as compared to NASA's MOD17 product (model RMSE of 6.98 vs. MODIS 7.46 GPP  $m^{-2}$ ). For the US-PLM site, Forbrich & Giblin (2015) took tidal inundation into account, finding that GPP was over-estimated by an average of less than 10%; their final model estimate was similar to the BC model for this site (Fig. S4). Schaefer et al. (2019) found that inclusion of tidal inundation resolved an additional 10 g C/ $m^2$ /yr out of  $\sim 1,800$  g C/ $m^2$ /yr, though the site was in a high marsh. The BC model achieved relatively similar or better improvements while aggregating biophysical parameterization across ten different sites. The Bayesian approach likely accounted for some of these improvements. Ultimately for the BC model or other CONUS-wide efforts, the limiting factor is that the input data does not exist. There are currently no inundation maps at the spatial or temporal scales required.

Meteorological variables that are available as layers in Google Earth Engine may hold better promise, such as Vapor Pressure Deficit (VPD) as used by MOD17, or better yet, precipitation from the same CFSV2 product that the BC model used for temperature and  $iPAR$  solar radiation. Rainfall and freshwater input are among the most important factors that drive tidal wetland productivity (Heinsch et al. 2004; Mendelsohn & Morris 2002; Feher et al. 2017; Chu et al. 2018), so the addition of these factors could provide improvements.

One advantage of utilizing the Bayesian framework is that any remaining variance in the posterior distribution of GPP is potentially captured by the remaining variables, namely by  $fPAR$  and its inputs  $m_{EVI}$  and EVI. For example, if rising salinity cannot be measured onsite, its effect on LUE and GPP can still be captured by observing the response of the plants in terms of reduced greenness with remotely sensed images. The lack of an explicit parameter does not mean that the variance it induced is not accounted for by the  $fPAR$  imagery inputs. Generally, the strength of an indirect capture of the variance by a parameter is most evident when relatively long-term data are available for parametrization, so that a wide variation of environmental conditions can be used to model the response in the posterior distribution. For example, soil salinity as measured by Barr et al. (2013) at the mangrove site is available for

more than a decade, and is also available at some locations that are proximate to other sites such as US-LA1 (CPRA 2019), but often such data do not exist at other tower sites. Thus, by compensating for missing input parameters indirectly, the Bayesian framework is relatively flexible, robust, and suited to broad scale analyses.

#### 4.5 Reducing BC Model Uncertainty

Static wetland boundaries were used as an input stream for the BC model. Yet, we know that these ecosystems evolve dynamically over time. Generally, when a tidal wetland erodes into water, the EVI is reduced. The BC model can capture this phenomenon.

However, tidal wetlands also migrate landward due to relative sea level change. The BC model did not calculate GPP landward of the static boundaries. Thus, newly-forming wetlands outside of these areas were not considered. Our maps also did not include wetlands that were restored or developed, unless they were already within the boundaries and the EVI detected the change. The net sum of these possibilities was that a non-interpolated version of the BC model likely under-estimated the CONUS GPP of tidal wetlands, as time moved forward from the date of the static wetland map.

However, the interpolation procedure gap-filled some eroding wetlands, particularly those that were small. As an example, the US-LA1 tower site was rapidly eroding and the BC model over-estimated its GPP. Land losses were  $\sim 4.1\%$  for coastal Louisiana from 2000-2016 (Couvillion et al 2017). In additional work outside the scope of the present study, we have noted that the CONUS-wide GPP appeared to be increasing over the 2000-2019 time period, although this result came with uncertainty. An initial investigation showed that  $\sim 1/3$  of the apparent GPP increase from 2000-2019 was due to interpolation. We are currently investigating this topic further, as other work has found increasing GPP over time for mangroves in Mexico (Vázquez-Lule et al. 2019). One potential future avenue is to use data from NOAA's Coastal Change Analysis Program (C-CAP) to map dynamic changes (Windham-Myers et al. 2018), although this approach could coarsen the spatial resolution and bring greater wetland classification errors.

The interpolation procedure introduced uncertainty into the GPP estimates at regional and CONUS-wide scales, but it also avoided severely under-counting GPP. For mixed pixels with  $< 80\%$  purity, there was a net benefit to interpolation. Interpolating across the 12 km distance was not particularly costly (the fit and  $r^2$  dropped  $\sim 0.07$ , although the average error as a percentage of the true value remained the same). Using a back-of-the-envelope calculation, the uncertainty due to interpolation across a 12 km distance was on the order of 20% (RMSE 1.47 g C interpolation across 12 km / RMSE 1.22 g C not across 12 km = 20%, comparing in absolute terms). The semi-variogram analysis showed a somewhat similar result, with a three-fold better estimate than using a random draw from all other GPP pixels. However, only  $\sim 11\%$  of pixels required interpolation across the 12 km distance or more. If we assume that the number and distances of the  $< 80\%$  purity pixels follow Fig. 5b, the uncertainty caused by the interpolation procedure was on the order of  $\sim 2.2\%$  for our CONUS-wide GPP estimate (or  $20\% * 11\% = 2.2\%$ ).

However more importantly, 24.5% of the CONUS tidal wetland area was missing from MODIS EVI datasets, and thus would otherwise be missing in calculated  $fPAR$  and GPP estimates. The interpolation procedure gap-filled these small wetland, mixed-pixel locations and obtained a more accurate estimate across the entirety of the CONUS. The cost was  $\sim 2.2\%$  uncertainty.

## 5. Conclusions

The BC model mapped tidal wetland GPP in a robust manner, matching field-derived EC tower observations with relatively low bias and error. Between 2000 and 2019, the average daily per m<sup>2</sup> GPP across all tidal wetlands and dates was  $4.32 \pm 2.45$  g C / m<sup>2</sup> / day. The total annual GPP for the entire continental US was  $39.65 \pm 0.89$  Tg/yr. The BC model provided GPP predictions at specific locations, as well as mapped the spatial arrangement of tidal wetland GPP across the continental US. The BC model provided improvements over NASA's MOD17 product by reducing error by approximately half when using the same EC flux tower data to compare ( $r^2$  of 0.83 versus 0.45, RMSE of 1.22 versus 3.38 g C / m<sup>2</sup> / day, average error 6% versus 15% off true value). Additionally, the BC model addressed the spatial issues associated with the relatively fine-scale tidal wetlands and their distribution across the broad extent of the entire US. It accounted for 24.5% of tidal wetland area, at the minimum, that was neglected by MOD17. The BC model accounted for over 16.8% of GPP that would still be neglected by other models that might use a similar 250 m resolution, by interpolating and accounting for MOD13Q1 EVI data that was otherwise missing for known wetland areas. The uncertainty due to interpolation was estimated at an average of 2.2%. The 16-day raster maps are publically-available at [daac.ornl.gov](https://daac.ornl.gov) and [www.data.gov](https://www.data.gov), and summary raster datasets, codes, and other files are publically-available at [bluecarbon.tamu.edu](https://bluecarbon.tamu.edu). We encourage other scientists to explore and use the BC model and maps to make new discoveries about tidal wetland GPP.

## Acknowledgements, Samples, and Data

EC tower data are available from AmeriFlux or from site PIs. The BC model 16-day raster maps are publically-available at [daac.ornl.gov](http://daac.ornl.gov) and [www.data.gov](http://www.data.gov), and summary raster datasets, codes, and other files are publically-available at [bluecarbon.tamu.edu](http://bluecarbon.tamu.edu).

We acknowledge the following AmeriFlux sites for their data records: US-SKR, US-NC4, US-PHM, US-SRR, US-PLM, US-HPY, US-STJ, US-VFP, US-LA1. Funding for AmeriFlux data resources was provided by the U.S. Department of Energy's Office of Science.

RAF acknowledges NASA's Carbon Cycle and Ecosystems Program (NNX14AM37G) and NASA's Carbon Monitoring System Program (NNH14AY671). IF and MA acknowledge the NSF LTER program (OCE 1237140, 1832178, OCE 1637630). KDK acknowledges the Ocean Carbon & Biogeochemistry Lateral Flux Synthesis and USGS LandCarbon Program. JSK acknowledges funding from USDA NIFA (2014-67003-22068), DOE NICCR (08-SC-NICCR-1072), and DOE LBNL (7090112). RV acknowledges NSF (NSF 1652594). JRP acknowledges NSF (GRFP DGE 1255832 and LTER DEB-1832221). JDF acknowledges NSF (DEB-1832221, DEB-1237517).

Any use of trade, firm, or product names is for descriptive purposes only and does not imply endorsement by the U.S. Government.

## References

- Artigas, F., Shin, J. Y., Hobbie, C., Marti-Donati, A., Schäfer, K. V. R., Pechmann, I. (2015). Long term carbon storage potential and CO<sub>2</sub> sink strength of a restored salt marsh in New Jersey. *Agricultural and Forest Meteorology*, 200, 313-321.
- Baldocchi, D. D., Hincks, B. B., & Meyers, T. P. (1988). Measuring Biosphere-Atmosphere Exchanges of Biologically Related Gases with Micrometeorological Methods. *Ecology*, 69, 1331-1340.
- Barba, J., Cueva, A., Bahn, M., Barron-Gafford, G.A., Bond-Lamberty, B., Hanson, P.J., Jaimes, A., Kulmala, L., Pumpanen, J., Scott, R.L., Wohlfahrt, G., Vargas, R. (2018). Comparing ecosystem and soil respiration: Review and key challenges of tower-based and soil measurements. *Agricultural and Forest Meteorology*, 249, 434-443.
- Barr, J. G., Engel, V., Smith, T. J., & Fuentes, J. D. (2012). Hurricane disturbance and recovery of energy balance, CO<sub>2</sub> fluxes and canopy structure in a mangrove forest of the Florida Everglades. *Agricultural and Forest Meteorology*, 153, 54-66.
- Barr, J. G., Engel, V., Fuentes, J. D., Fuller, D. O., & Kwon, H. (2013). Modeling light use efficiency in a subtropical mangrove forest equipped with CO<sub>2</sub> eddy covariance. *Biogeosciences*, 10, 2145-2158.
- Bartlett, D. S., Hardisky, M. A., Johnson, R. W., Gross, M. F., Klemas, V., & Hartman, J. M. (1988). Continental scale variability in vegetation reflectance and its relationship to canopy morphology. *International Journal of Remote Sensing*, 9(7), 1223-1241.
- Bianchi, T. S., Pennock, J., & Twilley, R. (Eds.) (1999). *Biogeochemistry of Gulf of Mexico Estuaries*. New York, John Wiley & Sons.
- Bianchi, T. S., Wysocki, L. A., Schneider, K. M., Filley, T. R., Corbett, D. R., & Kolker, A. (2011). Sources of terrestrial organic carbon in the Louisiana shelf (USA): Evidence for the importance of coastal marsh inputs. *Aquatic Geochemistry*, 17, 431-456.
- Bianchi, T. S., Feagin, R. A., Allison, M., Osburn, C. L., Arellano, A., Oviedo Vargas, D., Hinson, A., Eriksson, M., Morrison, E., & Barry, S. (2019). The fate and transport of allochthonous blue carbon in divergent coastal systems. In L. Windham-Myers, T. Troxler, S. Crooks (Eds.), *A Blue Carbon Primer: The State of Coastal Wetland Carbon Science, Practice, and Policy*. Boca Raton, London, CRC Press.
- Bond-Lamberty, B., Bailey, V. L., Chen, M., Gough, C. M., & Vargas, R. (2018). Globally rising soil heterotrophic respiration over recent decades. *Nature*, 560(7716), 80.
- Bridgman, S. D., Megonigal, J. P., Keller, J. K., Bliss, N. B., & Trettin, C. (2006). The carbon balance of North American wetlands. *Wetlands*, 26, 889-916.
- Bridgman, S. D., Megonigal, J. P., Keller, J. K., Bliss, N. B., Trettin, C. (2007) Wetlands. Chapter 13 and Appendix F in: (Eds) King A.W., Dilling L., Zimmerman G., Fairman D., Houghton R., Marland G., Rose A., Wilbanks T. *The first state of the carbon cycle report (SOCCR): The North American carbon budget and implications for the global carbon cycle*. U.S. Climate Change Science Program, Washington, DC, 139-148, 177-192.
- Byrd, K. B., Ballanti, L., Thomas, N., Nguyen, D., Holmquist, J. R., Simard, M., & Windham-Myers, L. (2018). A remote sensing-based model of tidal marsh aboveground

carbon stocks for the conterminous United States. *ISPRS Journal of Photogrammetry and Remote Sensing*, 139, 255-271.

Capooci, M., Barba, J., Seyfferth, A., & Vargas, R. (2019). Experimental influence of storm-surge salinity on soil greenhouse gas emissions from a tidal marsh. *Science of the Total Environment*, 686, 1164-1172.

Chmura, G. L., Anisfeld, S. C., Cahoon, D. R., & Lynch, J. C. (2003). Global carbon sequestration in tidal, saline wetland soils. *Global Biogeochemical Cycles*, 17, 1111, doi:10.1029/2002GB001917

Chmura, Gail L. (2013). What do we need to assess the sustainability of the tidal salt marsh carbon sink? *Ocean & Coastal Management*, 83, 25-31.

Chu, X. J., Han, G. X., Xing, Q. H., Xia, J. Y., Sun, B. Y., Yu, J. B., & Li, D. J. 2018. Dual effect of precipitation redistribution on net ecosystem CO<sub>2</sub> exchange of a coastal wetland in the Yellow River Delta. *Agricultural and Forest Meteorology*, 249, 286-296.

Couvillion, B. R., Beck, H., Schoolmaster, D., & Fischer, M. (2017). *Land area change in coastal Louisiana 1932 to 2016*. U.S. Geological Survey Scientific Investigations Map 3381, 16 p. <https://doi.org/10.3133/sim3381>.

Cowardin, L. M., Carter, V., Golet, F. C., & LaRoe, E. T. (1979). *Classification of Wetlands and Deepwater Habitats of the United States*. US Fish and Wildlife, Report No. FWS/OBS-78/31.

Crooks, S., Sutton-Grier, A. E., Troxler, T. G., Herold, N., Bernal, B., Schile-Beers, L., & Wirth, T. (2018). Coastal wetland management as a contribution to the US National Greenhouse Gas Inventory. *Nature Climate Change*, 8, 1109-1112.

CPRA. (2019). *Coastwide Reference Monitoring System-Wetlands Monitoring Data*. Coastal Protection and Restoration Authority (CPRA) of Louisiana. Available from: [https://www.lacoast.gov/crms/crms\\_public\\_data/publications/CRMS\\_FactSheet\\_Web.pdf](https://www.lacoast.gov/crms/crms_public_data/publications/CRMS_FactSheet_Web.pdf)

Desai, A. R., Richardson, A. D., Moffat, A. M., Kattge, J., Hollinger, D. Y., Barr, A., Falge E., Noormets, A., Papale, D., Reichstein, M., & Stauch, V.J. (2008). Cross-site evaluation of eddy covariance GPP and RE decomposition techniques. *Agricultural and Forest Meteorology*, 148, 821-838.

Didan, K., Barreto Munoz, A., Solano, R., & Huete, A. (2015). *MODIS Vegetation Index User's Guide (MOD13 Series)*. Version 3.00. <https://modis.gsfc.nasa.gov/data/dataproduct/mod13.php>

Duarte, C. M., Middelburg, J. J., Caracao, N. (2005). Major role of marine vegetation on the oceanic carbon cycle. *Biogeosciences*, 2, 1-8.

Duman, T., & Schäfer, K.V.R. (2018). Partitioning net ecosystem carbon exchange of native and invasive plant communities by vegetation cover in an urban tidal wetland in the New Jersey Meadowlands (USA). *Ecological Engineering*, 114, 16-24.

EPA. (2017) *Inventory of U.S. Greenhouse Gas Emissions and Sinks: 1990-2015*. U.S. Environmental Protection Agency, Washington, D.C.

Feher, L. C., Osland, M. J., Griffith, K. T., Grace, J. B., Howard, R. J., Stagg, C. L., Enwright, N. M., Krauss, K. W., Gabler, C. A., Day, R. H., & Rogers, K. (2017). Linear and nonlinear effects of temperature and precipitation on ecosystem properties in tidal saline wetlands. *Ecosphere*, 8(10), e01956.



Federal Geographic Data Committee. (2019). *Classification of Wetlands and Deepwater Habitats of the United States*. February 2019 version.  
[https://www.fws.gov/wetlands/documents/NWI\\_Wetlands\\_and\\_Deepwater\\_Map\\_Code\\_Diagram.pdf](https://www.fws.gov/wetlands/documents/NWI_Wetlands_and_Deepwater_Map_Code_Diagram.pdf)

Foken, T., Goeckede, M., Mauder, M., Mahrt, L., Amiro, B., & Munger W. (2004) Post-field data quality control. In X. Lee, W. Massman, B. Law (Eds.), *Handbook of Micrometeorology*.

Forbrich, I., & Giblin, A. E. (2015) Marsh-atmosphere CO<sub>2</sub> exchange in a New England salt marsh, *Journal of Geophysical Research: Biogeosciences*, 120, 1825-1838.

Forbrich, I., Giblin, A. E., & Hopkinson, C. S. (2018). Constraining marsh carbon budgets using long-term C burial and contemporary atmospheric CO<sub>2</sub> fluxes. *Journal of Geophysical Research: Biogeosciences*, 123, 867– 878.

Ghosh, S., Mishra, D. R., & Gitelson, A. A. (2016). Long-term monitoring of biophysical characteristics of tidal wetlands in the northern Gulf of Mexico – A methodological approach using MODIS. *Remote Sensing of the Environment*, 173, 39-58.

Gorelick, N., Hancher, M., Dixon, M., Ilyushchenko, S., Thau, D., & Moore, R. (2017). Google Earth Engine: Planetary-scale geospatial analysis for everyone. *Remote Sensing of the Environment*, 202, 18-27.

Hardisky, M. A., Gross, M. F., & Klemas, V. (1986). Remote sensing of coastal wetlands. *Bioscience*, 36, 453-460.

Hayes D. J., Vargas, R., Alin, S. R., Conant, R. T., Huttyra, L. R., Jacobson, A. R., Kurz, W. A., Liu, S., McGuire, A. D., Poulter, B., Woodall, C. W. (2018). Chapter 2: The North American carbon budget. In N. Cavallaro, G. Shrestha, R. Birdsey, M. A. Mayes, R. G. Najjar, S. C. Reed, P. Romero-Lankao, & Z. Zhu (Eds.), *Second State of the Carbon Cycle Report (SOCCR2): A Sustained Assessment Report*. U.S. Global Change Research Program, Washington, DC, USA, pp. 71-108.

Heilman, J. L., Cobos, D. R. Heinsch, F. A., Campbell, C. S., & McInnes, K.J. (1999). Tower-based conditional sampling for measuring ecosystem-scale carbon dioxide exchange in coastal wetlands. *Estuaries and Coasts*, 22, 584-591.

Heinsch, F. A., Reeves, M., Votava, P., Kang, S., Milesi, C., Zhao, M., Glassy, J., Jolly, W. M., Loehman, R., Bowker, C. F., Kimball, J. S., Nemani, R. R., & Running, S. W. (2003). *User's Guide. GPP and NPP (MOD17A2/A3) Products. MODIS Land Algorithm. Version. 2.0*. Available at: [https://lpdaac.usgs.gov/documents/212/mod17\\_v5\\_user\\_guide.pdf](https://lpdaac.usgs.gov/documents/212/mod17_v5_user_guide.pdf)

Heinsch, F. A., Heilman, J. L., McInnes, K. J., Cobos, D. R., Zuberer, D. A., & Roelke, D. L. (2004). Carbon dioxide exchange in a high marsh on the Texas Gulf Coast: Effects of freshwater availability. *Agricultural and Forest Meteorology*, 125, 159-172.

Heinsch, F. A., Zhao, M., Running, S. W., Kimball, J. S., Nemani, R. R., Davis, K. J., Bolstad, P. V., Cook, B. D., Desai, A. R., Ricciuto, D. M., Law, B. E., Oechel, W. C., Kwon, H., Luo, H., Wofsy, S. C., Dunn, A. L., Munger, J. W., Baldocchi, D. D., Xu, L., Hollinger, D. Y., Richardson, A. D., Stoy, P. C., Siqueira, M.B.S., Monson, R. K., Burns, S. P., & Flanagan, L. B. (2006). Evaluation of remote sensing based terrestrial productivity from MODIS using regional tower eddy flux network observations. *IEEE Transactions on Geoscience and Remote Sensing*, 44, 1908-1925.

Hiraishi, T., Krug, T., Tanabe, K., Srivastava, N., Baasansuren, J., Fukuda, M., & Troxler, T. (2014). *2013 Supplement to the 2006 IPCC Guidelines for National Greenhouse Gas Inventories: Wetlands*. IPCC, Switzerland.

Hinson, A. L., Feagin, R. A., Eriksson, M., Najjar, R. G., Herrmann, M., Bianchi, T. S., Kemp, M., Hutchings, J. A., Crooks, S., Boutton, T. (2017). The spatial distribution of soil organic carbon in tidal wetland soils of the continental United States. *Global Change Biology*, 23, 5468-5480.

Holmquist, J. R., Windham-Myers, L., Bliss, N., Crooks, S., Morris, J. T., Megonigal, J. P., Troxler, T., Weller, D., Callaway, J., Drexler, J., Ferner, M. C., Gonneea, M. E., Kroeger, K. D., Schile-Beers, L., Woo, I., Buffington, K., Breithaupt, J., Boyd, B. M., Brown, L. N., Dix, N., Hice, L., Horton, B. P., MacDonald, G. M., Moyer, R. P., Reay, W., Shaw, T., Smith, E., Smoak, J. M., Sommerfield, C., Thorne, K., Velinsky, D., Watson, E., Wilson Grimes, K., & Woodrey, M. (2018). Accuracy and precision of tidal wetland soil carbon mapping in the conterminous United States. *Scientific Reports*, 8, 9478.

Hopkinson, C. S., Cai, W. -J., & Hu, X. (2012). Carbon sequestration in wetland dominated coastal systems—a global sink of rapidly diminishing magnitude, *Current Opinion in Environmental Sustainability*, 4(2), 186-194.

Issaks, E. H., Srivastava, R. M. (1989). *An Introduction to Applied Geostatistics*. Oxford University Press, New York.

Kathilankal, J. C., Mozdzer, T. J., Fuentes, J. D. D'Odorico, P., McGlathery, K. J. & Zieman, J. C. (2008). Tidal influences on carbon assimilation by a salt marsh. *Environmental Research Letters* 3, 044010.

Keenan, T. F., Migliavacca, M., Papale, D., Baldocchi, D., Reichstein, M., Torn, M., Wutzler, T. (2019). Widespread inhibition of daytime ecosystem respiration. *Nature Ecology & Evolution*, 3, 407-415.

Klemas, V. (2011). Remote sensing of wetlands: Case studies comparing practical techniques. *Journal of Coastal Research*, 27, 418-427.

Knox, S. H., Windham-Myers, L., Anderson, F., Sturtevant, C., & Bergamaschi, B. (2018). Direct and indirect effects of tides on ecosystem-scale CO<sub>2</sub> exchange in a brackish tidal marsh in Northern California. *Journal of Geophysical Research Biogeosciences*, 123, 787-806.

Krauss, K. W., Holm, Jr., G. O., Perez, B. C., McWorter, D. E., Cormier, N., Moss, R. F., Johnson, D. J., Neubauer, S. C., & Raynie, R. C. (2016). Component greenhouse gas fluxes and radiative balance from two deltaic marshes in Louisiana: Pairing chamber techniques and eddy covariance. *Journal of Geophysical Research: Biogeosciences*, 121, 1503-1521.

Lasslop, G., Reichstein, M., Papale, D., Richardson, A. D., Arneeth, A., Barr, A., Stoy, P. & Wohlfahrt, G. (2010). Separation of net ecosystem exchange into assimilation and respiration using a light response curve approach: critical issues and global evaluation. *Global Change Biology*, 16, 187-208.

Lovelock, C. E., & Duarte, C. M. (2018). Dimensions of blue carbon and emerging perspectives. *Biology Letters*, 15, 20180781.

Malone, S. L., Starr, G., Staudhammer, C. L., & Ryan, M. G. (2013). Effects of simulated drought on the carbon balance of Everglades short-hydroperiod marsh. *Global Change Biology*, 19, 2511-2523.

- McLeod, E., Chmura, G. L., Bouillon, S., Salm, R., Bjork, M., Duarte, C. M., Lovelock, C. E., Schlesinger, W. H., & Silliman, B. R. (2011). A blueprint for blue carbon: toward an improved understanding of the role of vegetated coastal habitats in sequestering CO<sub>2</sub>. *Frontiers in Ecology and the Environment*, 9, 552-560.
- Mendelssohn, I. A., & Morris J., T. (2002). Eco-Physiological Controls on the Productivity of *Spartina Alterniflora* Loisel. In: M. P. Weinstein, D. A. Kreeger (Eds.) *Concepts and Controversies in Tidal Marsh Ecology*. Springer, Dordrecht.
- Miao, G., Noormets, A., Domec, J. C., Fuentes, M. F., Trettin, C. C., Sun, G., McNulty, S. G. and King, J. S. (2017). Hydrology and microtopography control carbon dynamics in wetlands: implications in partitioning ecosystem respiration in a coastal plain forested wetland. *Agricultural and Forest Meteorology*, 247, 343-355.
- Monteith, J. 1972. Solar radiation and productivity in tropical ecosystems. *Journal of Applied Ecology*, 9, 747-766.
- Murray, B. C., Pendleton, L., Jenkins, W. A., & Sifleet, S. (2011). *Green Payments for Blue Carbon: Economic Incentives for Protecting Threatened Coastal Habitats*. Report NI R 11-04, Nicholas Institute for Environmental Policy Solutions, Duke University, North Carolina, USA.
- Najjar, R. G., Herrmann, M., Alexander, R., Boyer, E. W., Burdige, D. J., Butman, D., Cai, W. -J., Canuel, E. A., Chen, R. F., Friedrichs, M. A. M., Feagin, R. A., Griffith, P. C., Hinson, A. L., Holmquist, J. R., Hu, X., Kemp, W. M., Kroeger, K. D., Mannino, A., McCallister, S. L., McGillis, W. R., Mulholland, M. R., Pilskaln, C. H., Salisbury, J., Signorini, S. R., St-Laurent, P., Tian, H., Tzortziou, M. A., Vlahos, P., Wang, Z. A., & Zimmerman, R. C. (2018). Carbon budget of tidal wetlands, estuaries, and shelf waters of Eastern North America. *Global Biogeochemical Cycles*, 32, 389-416.
- Nelleman, C., Corcoran, E., Duarte, C. M., Valdés, L., DeYoung, C., Fonseca, L., & Grimsditch, G. (Eds). (2009). *Blue Carbon: A Rapid Response Assessment*. United Nations Environment Programme, GRID-Arendal.
- NOAA. (2018). Coastal Assessment Framework – National Assessment of Estuary and Coastal Habitats. National Oceanic and Atmospheric Administration. Data available at: <https://catalog.data.gov/dataset/coastal-assessment-framework-national-assessment-of-estuary-and-coastal-habitats>
- O'Connell, J. L., Mishra, D. R., Cotton, D. L., Wang, L., Alber, M. (2017). The Tidal Marsh Inundation Index (TMII): An inundation filter to flag flooded pixels and improve MODIS tidal marsh vegetation time-series analysis. *Remote Sensing of Environment*, 201, 34-46.
- Papale, D., Reichstein, M., Aubinet, M., Canfora, E., Bernhofer, C., Kutsch, W., Longdoz, B., Rambal, S., Valentini, R., Vesala, T., & Yakir, D. (2006). Towards a standardized processing of Net Ecosystem Exchange measured with eddy covariance technique: algorithms and uncertainty estimation, *Biogeosciences*, 3, 571-583.
- Reichstein, M., Falge, E., Baldocchi, D., Papale, D., Aubinet, M., Berbigier, P., Bernhofer, C., Buchmann, N., Gilmanov, T., Granier, A., Grünwald, T., Havránková, K., Ilvesniemi, H., Janous, D., Knohl, A., Laurila, T., Lohila, A., Loustau, D., Matteucci, G., Meyers, T., Miglietta, F., Ourcival, J., Pumpanen, J., Rambal, S., Rotenberg, E., Sanz, M., Tenhunen, J., Seufert, G., Vaccari, F., Vesala, T., Yakir, D., & Valentini, R. (2005). On the separation of net ecosystem exchange into assimilation and ecosystem respiration: review and improved algorithm. *Global Change Biology*, 11, 1424-1439.

Rocha, A. V., & Goulden, M. L. (2009). Why is marsh productivity so high? New insights from eddy covariance and biomass measurements in a *Typha* marsh. *Agricultural and Forest Meteorology*, 149, 159-168.

Running, S. W., Nemani, R. R., Heinsch, F., Zhao, M., Reeves, M., Hasimoto, H. (2004). A continuous satellite-derived measured of global terrestrial primary productivity: Future science and applications. *Bioscience*, 56, 547-560.

Saha, S., Moorthi, S., Wu, X., Wang, J., Nadiga, S., Tripp, P., Behringer, D., Hou, Y -T, Chuang, H -Y, Iredell, M., Ek, M., Meng, J., Yang, R., Peña Mendez, M., van den Dool, H., Zhang, Q, Wang, W., Chen, M., & Becker, E. (2014). The NCEP Climate Forecast System Version 2. *Journal of Climate*, 27, 2185-2208.

Schäfer, K. V. R., Duman, T., Tomasicchio, K., Tripathee, R., & Sturtevant, C. (2019). Carbon dioxide fluxes of temperate urban wetlands with different restoration history. *Agricultural and Forest Meteorology*, 275, 223-232.

Schile, L. M., Byrd, K. B., Windham-Myers, L., & Kelly, M. (2013). Accounting for non-photosynthetic vegetation in remote-sensing-based estimates of carbon flux in wetlands. *Remote Sensing Letters*, 4, 542-551.

Taiz, L., & Zeiger, E. (2002). *Plant Physiology*. Third edition, Sinauer Associates, Inc., Publishers, Sunderland, Massachusetts, USA. 690 pp.

Tao, J., Mishra, D. R., Cotton, D. L., O'Connell, J., Leclerc, M., Binti Nahrawi, H., Zhang, G., & Pahari, R. (2018). A comparison between the MODIS product (MOD17A2) and a tide-robust empirical GPP model evaluated in a Georgia wetland. *Remote Sensing*, 10, 10.3390.

Troxler, T. G., Barr, J. G., Fuentes, J. D., Engel, V., Anderson, G., Sanchez, C., Lagomasino, D., Price, R., & Davis, S. E (2015). Component-specific dynamics of riverine mangrove CO<sub>2</sub> efflux in the Florida coastal Everglades. *Agricultural and Forest Meteorology*, 213, 273-282.

Vázquez-Lule, A., Colditz, R., Herrera-Silveira, J., Guevara, M., Rodriguez-Zuniga, M., Cruz, I., Ressi, R., & Vargas, R. (2019). Greenness trends and carbon stocks of mangroves across Mexico. *Environmental Research Letters*: In press. <https://doi.org/10.1088/1748-9326/ab246e>

Wang, S. R., Di Iorio, D., Cai, W- J., Hopkinson, C. S. 2018. Inorganic carbon and oxygen dynamics in a marsh-dominated estuary. *Limnology and Oceanography*, 63, 47-71.

Wehr, R., Munger, J. W., McManus, J. B., Nelson, D. D., Zahniser, M. S., Davidson, E. A., Wofsy, S. C., & Saleska, S. R. (2016). Seasonality of temperate forest photosynthesis and daytime respiration. *Nature*, 534, 680.

Wieski, K., & Pennings, S.C. (2014). Climate drivers of *Spartina alterniflora* saltmarsh production in Georgia, USA. *Ecosystems*, 17, 473-484.

Windham-Myers, L., Cai, W. -J., Alin, S. R., Andersson, A., Crosswell, J., Dunton, K. H., Hernandez-Ayon, J. M., Herrmann, M., Hinson, A. L., Hopkinson, C. S., Howard, J., Hu, X., Knox, S. H., Kroeger, K., Lagomasino, D., Magonigal, P., Najjar, R. G., Paulsen, M.-L., Peteet, D., Pidgeon, E., Schäfer, K. V. R., Tzortziou, M., Wang, Z. A., & Watson, E. B. (2018) Chapter 15: Tidal wetlands and estuaries. In N. Cavallaro, G. Shrestha, R. Birdsey, M. A. Mayes, R. G. Najjar, S. C. Reed, P. Romero-Lankao, & Z. Zhu (Eds.), *Second State of the Carbon Cycle Report (SOCCR2): A Sustained Assessment Report*. U.S. Global Change Research Program, Washington, DC, USA, pp. 596-648.

Accepted Article

Wutzler, T., Lucas-Moffat, A., Migliavacca, M., Knauer, J., Sickel, K., Šigut, L., Menzer, O., & Reichstein, M. (2018). Basic and extensible post-processing of eddy covariance flux data with REdDyProc. *Biogeosciences*, 15, 5015-5030.

Zhao, M., Heinsch, F.A., Nemani, R. R., & Running, S. W. (2005). Improvements of the MODIS terrestrial gross and net primary production global data set. *Remote Sensing of Environment*, 95, 164–176.

Zhao, J., Malone, S. L., Oberbauer, S. F., Olivas, P. C., Schedlbauer, J. L., Staudhammer, C. L., & Starr, G. (2019). Intensified inundation shifts a freshwater wetland from a CO<sub>2</sub> sink to a source. *Global Change Biology*, 25, 3333.

**Table 1.** Summary of flux data sets used during parameterization and validation of the

EC Tower Site ID, Name (State)	Location (Lat, Lon)	Example Reference	Instrumentation, Partitioning	Dominant Plant Species	
US-SKR, Shark River Slough Everglades (Florida)	25.363293, -81.077544	Barr et al. 2013	CSAT, LI7500, Site Specific	<i>Rhizophora mangle</i> , <i>Avicennia germinans</i> , <i>Laguncularia racemosa</i>	Woo
US-NC4, Alligator River (North Carolina)	35.787717, -75.903952	Miao et al. 2017	Windmaster, LI-7500A, LI-7200, Site Specific	<i>Taxodium distichum</i> , <i>Nyssa aquatica</i> , <i>Acer rubrum</i>	Woo
US-PHM, Plum Island High Marsh (Massachusetts)	42.742443, -70.830219	Forbrich et al. 2018	CSAT, EC155, Reichstein et al. (2005)	<i>Spartina patens</i> , <i>Spartina alterniflora</i> , <i>Distichlis spicata</i>	Herb
US-SRR, Suisun Marsh - Rush Ranch (California)	38.200556, -122.02635	Knox et al. 2018	Gill, LI7500A, Site Specific	<i>Schoenoplectus</i> spp., <i>Typha</i> spp., <i>Lepidium latifolium</i> L.	Herb
US-PLM, Plum Island Low Marsh (Massachusetts)	42.734463, -70.838231	N/A	CSAT, EC155 Reichstein et al. (2005)	<i>Spartina alterniflora</i>	Herb
US-HPY, Hawk Property (New Jersey)	40.769173, -74.085318	Duman & Schäfer 2018	CSAT, LI7500A, Site Specific	<i>Spartina patens</i> , <i>Phragmites australis</i>	Herb
US-STJ, St. Jones Reserve (Delaware)	39.088225, -75.437210	Capooci et al. 2019	Gill, LI7200 Reichstein et al. (2005)	<i>Spartina alterniflora</i> , <i>Spartina cynosuroides</i>	Herb
US-VFP, Virginia Coast Res. Following Point (Virginia)	37.411065, -75.833208	N/A	Gill, LI7500A Reichstein et al. (2005)	<i>Spartina alterniflora</i>	Herb
GCE, Georgia Coastal Ecosystems LTER (Georgia)	31.444094, -81.283444	Tao et al. 2018	CSAT, LI7200, Site Specific	<i>Spartina alterniflora</i>	Herb
US-LA1, Pointe-aux-Chenes Brackish Marsh (Louisiana)	29.501303, -90.444897	Krauss et al. 2016	Gill, LI7200 Reichstein et al. (2005)	<i>Spartina patens</i>	Herb

Bayesian framework and BC model.

<sup>1</sup> Codes denote how each year of EC tower field-derived data was used for the final two class model (woody and herbaceous classes): P=parameterization of Bayesian framework only, V=validation for Bayesian framework and BC model, N=validation for BC model use only, O='offsite' validation for BC model use only

**Table 2.** Bayesian framework validation, for two-class (woody vs. herbaceous) and four-class (woody mangrove, woody swamp, herbaceous salt marsh, herbaceous freshwater) parameterizations, and when including or excluding light saturation coefficients.

		Including light saturation coefficient				Excluding light saturation coefficient			
		Tidal Woody		Tidal Herbaceous		Tidal Woody		Tidal Herbaceous	
r <sup>2</sup> slope offset RMSE n	r <sup>2</sup>	0.74		0.93		0.08		0.93	
	slope	0.68		0.89		0.26		0.89	
	offset	0.13		0.01		0.31		0.01	
	RMSE	0.08		0.07		0.17		0.07	
	n	136		84		136		84	
		Woody Mangrove	Woody Swamp	Herbaceous Salt Marsh	Herbaceous Freshwater	Woody Mangrove	Woody Swamp	Herbaceous Salt Marsh	Herbaceous Freshwater
r <sup>2</sup> slope offset RMSE n	r <sup>2</sup>	0.65	0.83	0.96	0.87	0.21	0.80	0.96	0.84
	slope	0.46	0.97	1.04	0.94	0.35	1.01	1.00	0.90
	offset	0.25	0.01	0.01	0.03	0.30	0.01	0.01	0.04
	RMSE	0.05	0.1	0.04	0.09	0.09	0.11	0.04	0.10
	n	46	22	21	22	46	22	21	22

**Table 3.** Bayesian framework validation for the mangrove class, with and without salinity, and when using the median versus the mean of the Bayesian distribution for each parameterized value.

value	Excluding salinity coefficient		Including salinity coefficient
	Mean	Median	Median
$r^2$	0.34	0.65	0.65
slope	0.73	0.46	0.47
offset	0.16	0.25	0.25
RMSE	0.12	0.05	0.05
n	92	46	46



**Table 4.** Final Bayesian distribution framework look-up tables used by the BC model for the woody and herbaceous tidal wetland classes. Units for  $\epsilon_0$  are mmol C / mol photons.  $m_{PAR}$  and  $m_{EVI}$  are dimensionless.

Woody Tidal Wetlands					
	mean	std. dev.	2.5%	median 50%	97.5%
$\epsilon_0$	39.63	21.23	24.38	31.21	109.3
$m_{EVI}$	2.81	1.15	0.6	2.99	4.79
$T_{min}$ (°C)	0.11	2.75	-7.07	1.04	3.01
$T_{max}$ (°C)	33.99	1.9	30.82	33.68	38.81
$T_{opt}$ (°C)	28.95	1.77	27.09	28.43	34.38
$m_{PAR}$	0.0098	0.0007	0.0083	0.0098	0.011
Herbaceous Tidal Wetlands					
	mean	std. dev.	2.5%	median 50%	97.5%
$\epsilon_0$	23.34	9.5	12.54	21.03	48.19
$m_{EVI}$	3.03	1.05	1.11	3.1	5.06
$T_{min}$ (°C)	-0.16	2.31	-5.71	0.4	2.75
$T_{max}$ (°C)	33.46	2.22	28.19	33.47	38.35
$T_{opt}$ (°C)	27.74	2.47	22.52	27.74	33.93
$m_{PAR}$	-0.002	0.004	-0.012	-0.002	0.004

**Table 5.** Top 20 estuaries, ranked in the order of total annual GPP. Statistics based on average over 2000-2019. GPP per m<sup>2</sup> is the average for the tidal wetlands only within each estuary.

Estuary Name	State	Area (km <sup>2</sup> )	GPP per m <sup>2</sup> (g C / m <sup>2</sup> / d)	Total GPP (Tg C / yr)
1. Atchafalaya/Vermilion Bays	LA	2465	5.24	4.72 ± 0.14
2. Chesapeake Bay	MD, VA, DC, PA	1651	3.56	2.15 ± 0.11
3. Breton/Chandeleur Sound	LA	1247	4.35	1.98 ± 0.12
4. North Ten Thousand Islands	FL	925	5.82	1.97 ± 0.07
5. South Ten Thousand Islands	FL	894	5.83	1.90 ± 0.07
6. Barataria Bay	LA	1151	3.96	1.66 ± 0.06
7. Mermentau River	LA	777	5.56	1.58 ± 0.10
8. Terrebonne/Timbalier Bays	LA	1156	3.43	1.45 ± 0.07
9. West Mississippi Sound	LA	780	4.78	1.36 ± 0.05
10. Calcasieu Lake	LA	667	4.64	1.13 ± 0.10
11. Sabine Lake	LA, TX	593	5.01	1.08 ± 0.06
12. Pamlico Sound	NC	648	4.18	0.99 ± 0.04
13. Delaware Bay	DE, NJ	699	3.46	0.88 ± 0.05
14. St. Andrew/St. Simons Sounds	GA	552	4.10	0.83 ± 0.03
15. St. Catherines/Sapelo Sounds	GA	532	3.35	0.65 ± 0.03
16. Florida Bay	FL	330	5.36	0.64 ± 0.03
17. Winyah Bay	SC	340	5.19	0.64 ± 0.03
18. Galveston Bay	TX	347	4.68	0.59 ± 0.03
19. Albemarle Sound	NC, VA	357	4.48	0.58 ± 0.03
20. Mississippi River	LA	423	3.40	0.52 ± 0.03

Figure 1

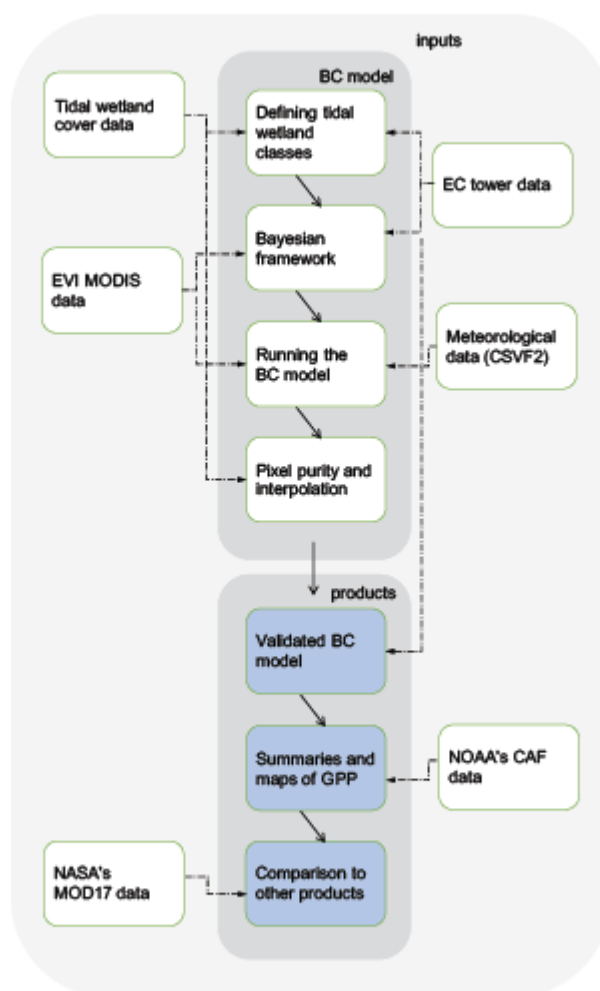


Fig. 1. Overview of the input datasets, processes, and products of the BC model.

**Figure 2**

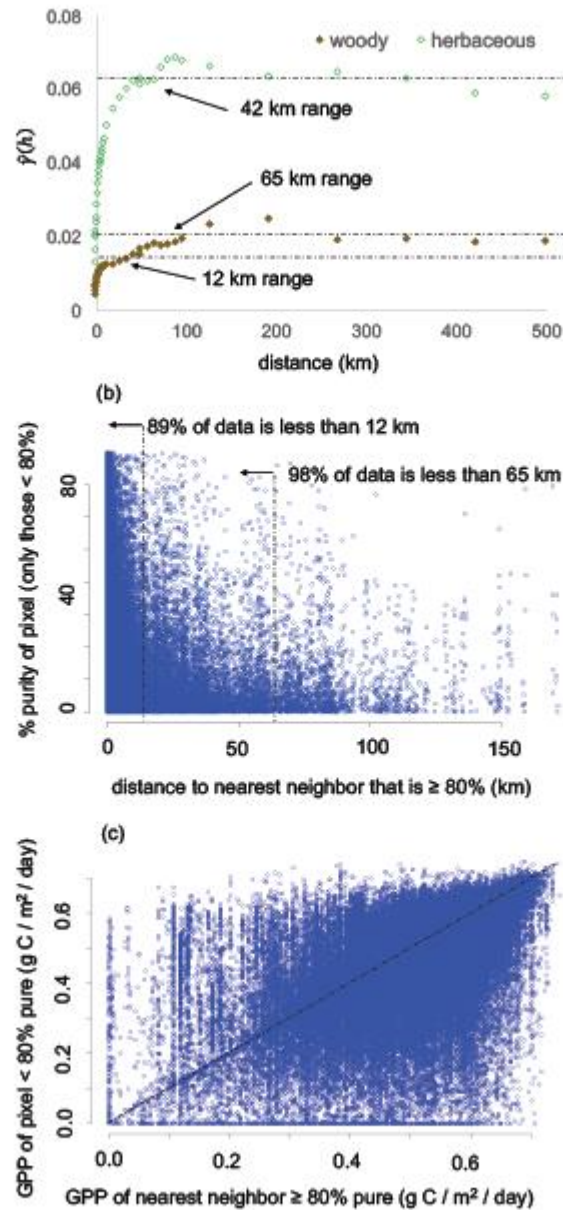


Fig. 2. Pixel purity and interpolation analysis, including: (a) Semi-variogram for woody and herbaceous tidal wetlands, showing 12 km as the limiting distance over which interpolation is optimized for the woody class, (b) distribution of the <80% purity pixels across distance from  $\geq 80\%$  purity pixels, showing that over 89% are less than 12 km away, (c) GPP of  $\geq 80\%$  purity nearest neighbor, for <80% purity pixels, showing potential correction afforded by interpolation. Dotted lines in (c) denotes 1:1 line.

**Figure 3**

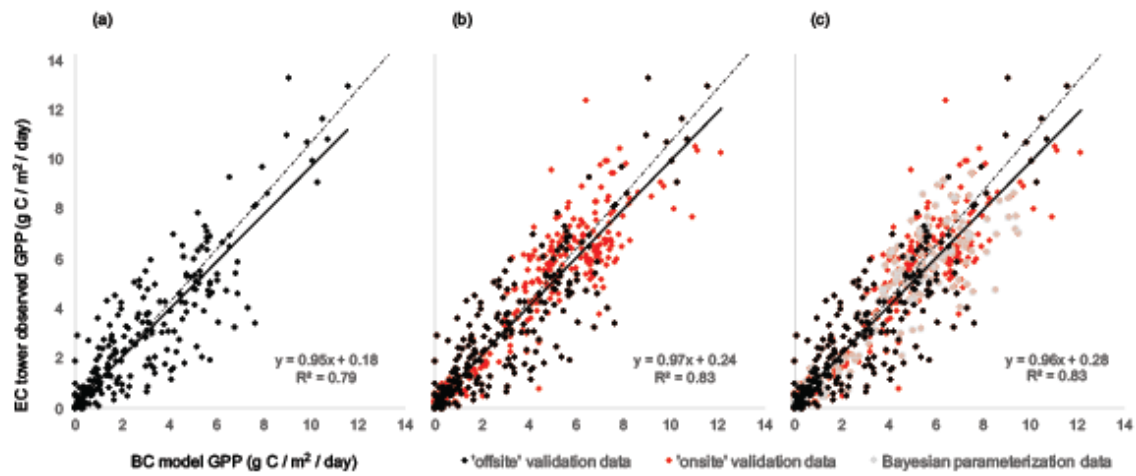


Fig. 3. BC model predicted GPP versus field-derived EC tower GPP, using (a) only validation data from the six 'offsite' tower locations, (b) all validation data from the ten tower locations excluding, and (c) including the dates also used in the parameterization of the Bayesian framework.

**Figure 4**

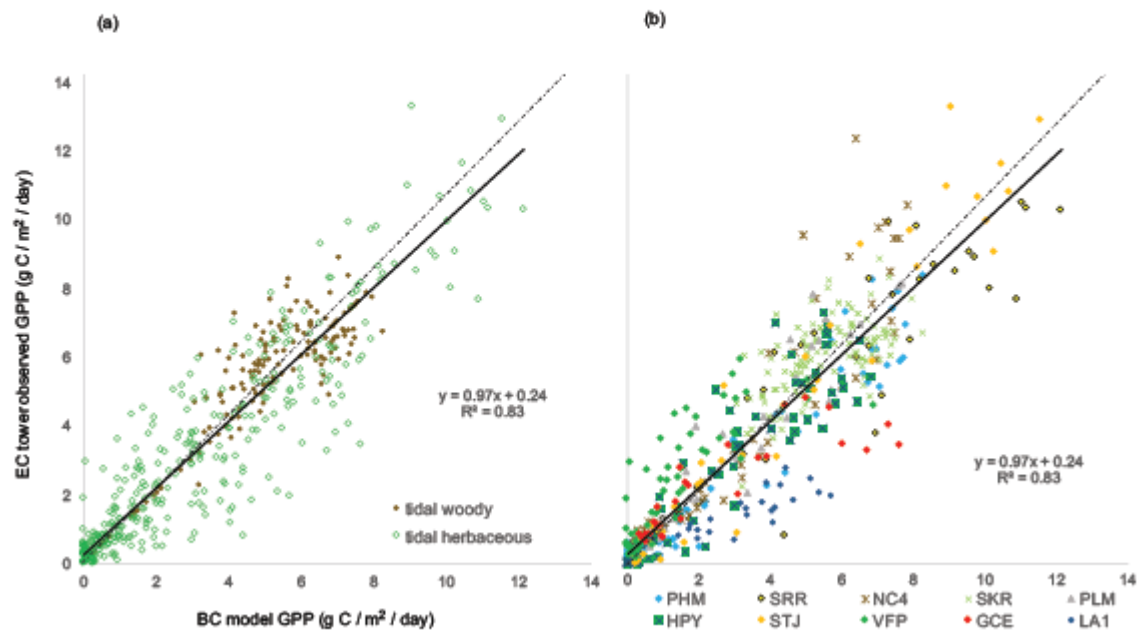


Fig. 4. BC model predicted versus field-derived EC tower GPP for (a) tidal woody versus herbaceous wetlands, and (b) the various towers used for validation.

Figure 5

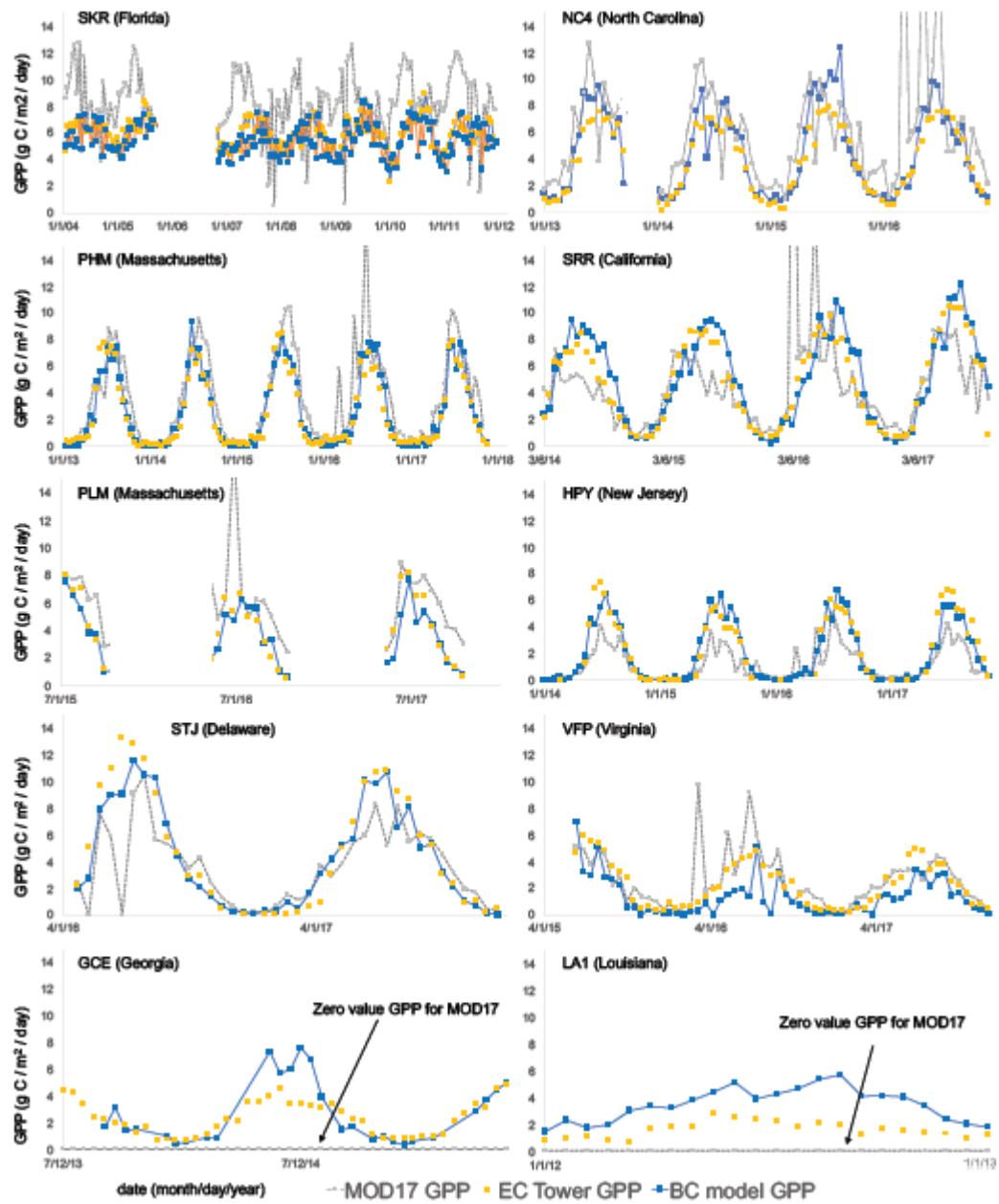


Fig. 5. BC model GPP, MOD17 model GPP, and field-derived EC tower GPP at the ten sites.

Figure 6

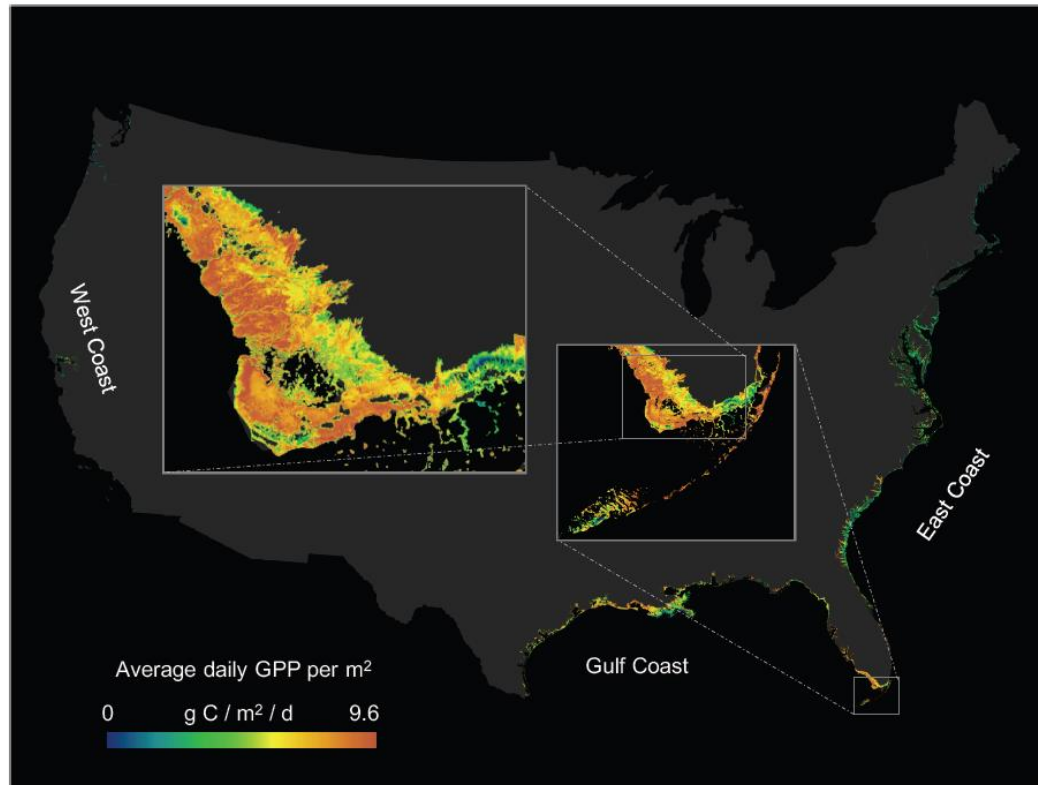


Fig. 6. Average daily GPP per  $\text{m}^2$  across the continental US, 2000-2019. Data constructed from averaging all 16-day periods. As an example of spatial resolution, zoom boxes detail the the North and South Ten Thousand Islands in the Florida Everglades.



**Figure 7**

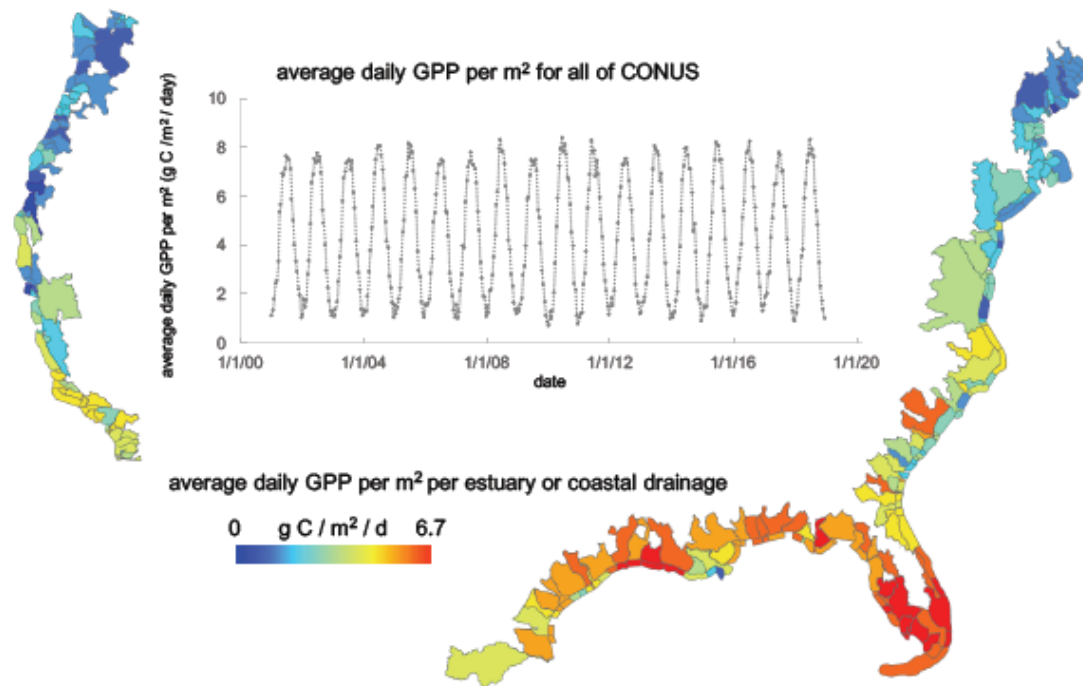


Fig. 7. The average daily GPP per m<sup>2</sup>, shown at 16-day intervals across all tidal wetlands in the continental US from 2000-2019. The map details the averages within individual estuarine and coastal drainage basins (EDAs/CDAs).

**Figure 8**

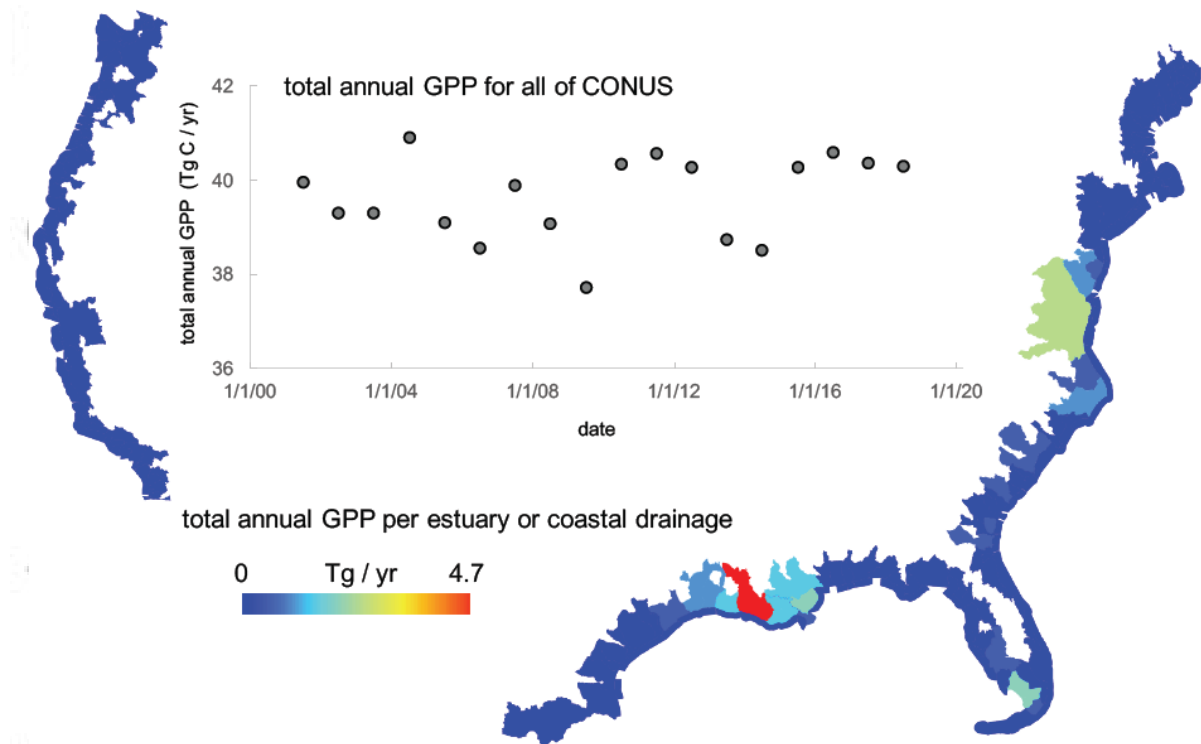


Fig. 8. The total annual GPP, shown at annual intervals across all tidal wetlands in the continental US from 2000-2019. The map details the sum totals within individual estuarine and coastal drainage basins (EDAs/CDAs).

Figure 9

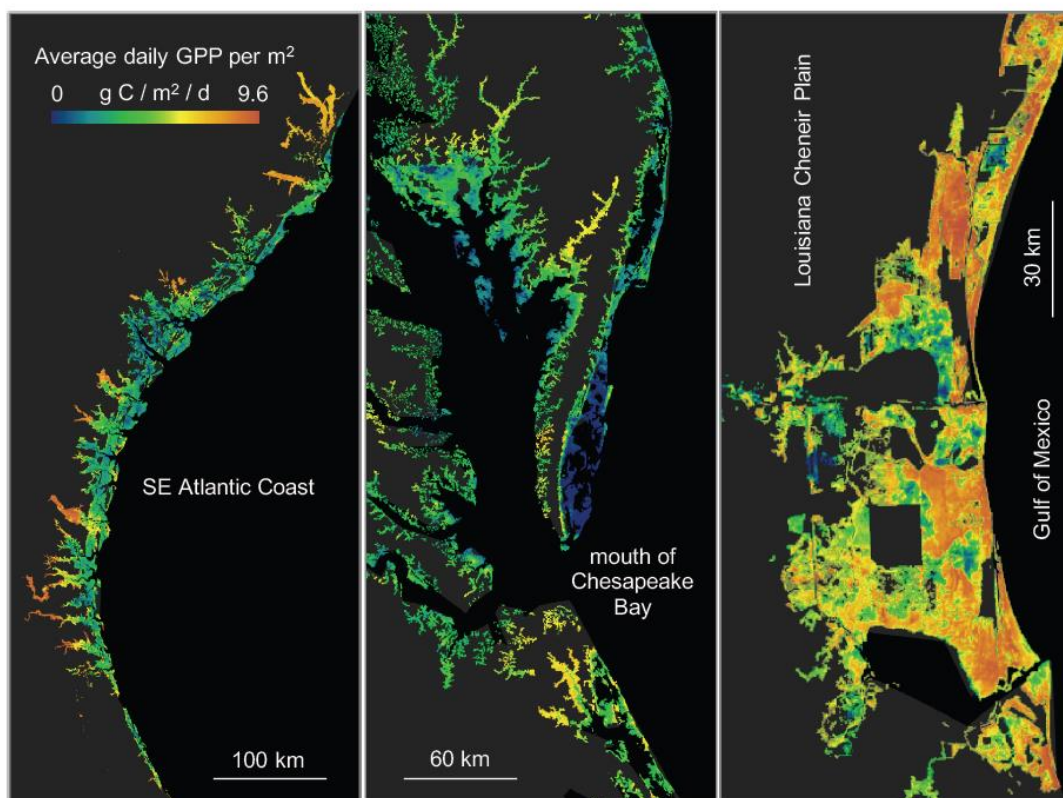


Fig. 9. Examples of spatial patterns in the distribution of average daily GPP per m<sup>2</sup> across selected regions of the continental US. The apparent patterns could be related to freshwater inflow gradients on the SE Atlantic Coast (left), oceanic influences on barrier island marshes versus internal Chesapeake Bay marshes (middle), and hydrologic or other types of management on the Louisiana Chenier Plain (right, rotated). Data constructed from averaging all 16-day periods.